



HAL
open science

Identifying footpoints of pre-eruptive and coronal mass ejection flux ropes with sunspot scars

Chen Xing, Guillaume Aulanier, Brigitte Schmieder, Xin Cheng, Mingde Ding

► To cite this version:

Chen Xing, Guillaume Aulanier, Brigitte Schmieder, Xin Cheng, Mingde Ding. Identifying footpoints of pre-eruptive and coronal mass ejection flux ropes with sunspot scars. *Astronomy and Astrophysics* - A&A, 2024, 682, pp.A3. 10.1051/0004-6361/202347053 . hal-04441290

HAL Id: hal-04441290

<https://hal.science/hal-04441290>

Submitted on 15 Mar 2024

HAL is a multi-disciplinary open access archive for the deposit and dissemination of scientific research documents, whether they are published or not. The documents may come from teaching and research institutions in France or abroad, or from public or private research centers.

L'archive ouverte pluridisciplinaire **HAL**, est destinée au dépôt et à la diffusion de documents scientifiques de niveau recherche, publiés ou non, émanant des établissements d'enseignement et de recherche français ou étrangers, des laboratoires publics ou privés.



Distributed under a Creative Commons Attribution 4.0 International License

Identifying footpoints of pre-eruptive and coronal mass ejection flux ropes with sunspot scars[★]

Chen Xing^{1,2}, Guillaume Aulanier^{1,3}, Brigitte Schmieder^{4,5,6}, Xin Cheng², and Mingde Ding²

¹ Sorbonne Université, Observatoire de Paris-PSL, École Polytechnique, IP Paris, CNRS, Laboratoire de Physique des Plasmas, Paris, France

² School of Astronomy and Space Science, Nanjing University, Nanjing, PR China
e-mail: chenxing@smail.nju.edu.cn

³ Rosseland Centre for Solar Physics (RoCS), Institute of Theoretical Astrophysics, Universitetet i Oslo, Oslo, Norway

⁴ LESIA, Observatoire de Paris, Université PSL, CNRS, Sorbonne Université, Université de Paris, 5 place Jules Janssen, 92190 Meudon, France

⁵ Centre for Mathematical Plasma Astrophysics, Dept. of Mathematics, KU Leuven, 3001 Leuven, Belgium

⁶ SUPA, School of Physics & Astronomy, University of Glasgow, Glasgow G12 8QQ, UK

Received 30 May 2023 / Accepted 19 October 2023

ABSTRACT

Context. The properties of pre-eruptive structures and coronal mass ejections (CMEs) are characterized by those of their footpoints, the latter of which attract a great deal of interest. However, the matter of how to identify the footpoints of pre-eruptive structures and how to do so with the use of ground-based instruments still remains elusive.

Aims. In this work, we study an arc-shaped structure intruding in the sunspot umbra. It is located close to the (pre-)eruptive flux rope footpoint and it is expected to help identify the footpoint.

Methods. We analyzed this arc-shaped structure, which we call a “sunspot scar”, in a CME event on July 12, 2012, and in two CME events from observationally inspired magnetohydrodynamic simulations performed by OHM and MPI-AMRVAC.

Results. The sunspot scar displays a more inclined magnetic field with a weaker vertical component and a stronger horizontal component relative to that in the surrounding umbra and is manifested as a light bridge in the white light passband. The hot field lines anchored in the sunspot scar are spatially at the transition between the flux rope and the background coronal loops and temporally in the process of the slipping reconnection which builds up the flux rope.

Conclusions. The sunspot scar and its related light bridge mark the edge of the CME flux rope footpoint and particularly indicate the edge of the pre-eruptive flux rope footpoint in the framework of “pre-eruptive structures being flux ropes”. Therefore, they provide a new perspective for the identification of pre-eruptive and CME flux rope footpoints, as well as new methods for studying the properties and evolution of pre-eruptive structures and CMEs with photospheric observations only.

Key words. Sun: corona – Sun: coronal mass ejections (CMEs) – Sun: flares – sunspots

1. Introduction

The Sun frequently releases rapid ejections of plasmas, known as coronal mass ejections (CMEs), into interplanetary space. When CMEs propagate close to the Earth and interact with the Earth’s magnetosphere, they potentially induce damage to human high-tech activities such as satellite communications and power transmission (Elovaara 2007). The forecast of CMEs, which is important to prevent these space hazards, relies on a thorough understanding of the properties of CMEs. Generally, it is considered that the flux rope in which magnetic field lines are intertwined with each other is the main magnetic configuration of the CME (Chen et al. 1997; Dere et al. 1999); it is even likely to make up the pre-eruptive structure of many CMEs (see the reviews by Cheng et al. 2017 and Patsourakos et al. 2020), as evidenced by the filament (Aulanier & Demoulin 1998; Guo et al. 2010; Schmieder et al. 2013) and the hot channel (Cheng et al. 2012; Zhang et al. 2012).

The footpoints of flux ropes, taking advantage of their measurable magnetic field and close links to pre-eruptive structures and CMEs, make great contributions to understanding the

properties and evolution of these (pre-)eruptive structures. For example, with the magnetic field in the identified footpoints, Wang et al. (2019, 2017) showed the increase in the twist of pre-eruptive and CME flux ropes, which demonstrates the building up of these structures. During the eruption, the drifting and deformation of CME footpoints could reveal magnetic reconnection processes related to the CME evolution (Aulanier & Dudík 2019; Gou et al. 2023). These processes are further supported by the evolution of the toroidal flux in the CME footpoint (Xing et al. 2020). Furthermore, before CMEs pass the Alfvénic surface in the solar wind, the conditions of CME footpoints always have effects on the shape and extension of CMEs, as the magnetic tension force can still propagate all along CMEs then. Lastly, the location and shape of footpoints and the magnetic field in footpoints are also essential input parameters in many extrapolation methods for reconstructing the coronal magnetic field in the pre-eruptive flux rope, for example, the flux rope insertion method (Su et al. 2011) and the regularized Biot–Savart law method (Titov et al. 2021; Guo et al. 2023). An accurate identification of the flux rope footpoints, as the basis of these works, is thus extremely important.

So far, two methods have been proposed to identify CME footpoints in observations. First, the two footpoints of the CME

[★] Movies associated to Figs 2, 4, 8, and 10 are available at <https://www.aanda.org>

flux rope are considered to correspond to a pair of core dimming regions where the extreme ultraviolet (EUV) intensity is significantly reduced during the eruption (Sterling & Hudson 1997; Cheng & Qiu 2016; Wang et al. 2017). The core dimming is believed to be caused by the plasma rarefaction in the CME foot as a result of the flux rope eruption and expansion (Harra & Sterling 2001; Tian et al. 2012), or by the temporary generation of a transient solar wind at the footpoints of the CME expanding field lines (Lörinčák et al. 2021). Second, the CME footpoint is usually identified as the region (partially) enclosed by the hooked part of the flare ribbon (Wang et al. 2017; Aulanier & Dudík 2019), as the footprint of the quasi-separatrix layers (QSLs; Priest & Démoulin 1995) is well matched with both the flare ribbon hook (Savcheva et al. 2015; Zhao et al. 2016) and the boundary of the flux rope footpoint (Démoulin et al. 1996; Janvier et al. 2014). In addition, some recent works also identify the footpoint with a combination of these two features (e.g., Xing et al. 2020). However, we note that on the one hand, these two methods are usually only applicable to CMEs rather than pre-eruptive structures, as the core dimming and the flare ribbon are accompanying phenomena of the eruption. On the other hand, the pre-eruptive flux rope footpoint is not always the same as the CME footpoint. This is because the footpoint is built up under the magnetic reconnection among overlying field lines (Aulanier & Dudík 2019) and deformed under the magnetic reconnection in the flux rope and that between the flux rope and the overlying field (Aulanier & Dudík 2019; Gou et al. 2023) during the eruption. Therefore, it remains still elusive to identify the footpoints of pre-eruptive structures of CMEs.

Recent studies have shown that the CME evolution in the corona could influence the photospheric magnetic field, that is, the so called “the tail wagging the dog” phenomenon (Aulanier 2016). For example, the photospheric magnetic field is found to become more horizontal close to the polarity inversion line (PIL) of the CME source region (Sun et al. 2012; Wang et al. 2012a), while it appears more vertical in the periphery of the source region (Liu et al. 2005; Wang et al. 2012b) after the eruption. The change in the magnetic field may result from that the energy released during the eruption induces a reduction of the magnetic pressure in the core of the active region (Wang et al. 2012b). Recently, Barczynski et al. (2019) offered another explanation for these changes, namely, that the more horizontal field close to the PIL is due to the reconnection-driven contraction of post-flare loops and the more vertical field in the periphery is a result of the CME-driven stretching of coronal loops. A similar idea is also proposed by Cheng & Ding (2016) that the stretching of CME legs leads to the photospheric magnetic field becoming more vertical. The influence of the CME evolution on the photosphere is even manifested in the white light passband, showing as the penumbra darkened near the PIL, whereas it is weakened in the outer periphery of sunspots (Liu et al. 2005; Wang et al. 2012b). In addition, Wang & Liu (2021) showed that the magnetic reconnection during the erosion-stage of the CME eruption could lead to an enhancement of both the vertical and horizontal components of the photospheric magnetic field in the ribbon-swept region. We note that all of the above results suggest that the features of the photospheric magnetic field in the CME source regions may reflect the properties and evolution of CMEs.

In this work, we demonstrate such a phenomenon that an arc-shaped structure intruding in the sunspot umbra marks the footpoint edge of the pre-eruptive flux rope of the CME, in both observations and simulations. The simulations even suggest that this structure marks the footpoint edge for the flux rope during the eruption. We highlight that this is a new perspective

for identifying the flux rope footpoints, applicable to both the ground-based and space-based telescopes. In the following, we show this phenomenon in observations in Sect. 2 and then in simulations in Sect. 3. We also demonstrate the nature of this phenomenon in Sect. 3, followed by a summary in Sect. 4. A discussion is presented in Sect. 5.

2. Sunspot scar in a CME-flare event on July 12, 2012

2.1. Data

In this section, we study this arc-shaped structure in a CME-flare event on July 12, 2012. The evolution of this event is exhibited by EUV images at 131 Å and 304 Å passbands, which are observed by Atmospheric Imaging Assembly (AIA; Lemen et al. 2012) on board Solar Dynamics Observatory (SDO; Pesnell et al. 2012), and also Spaceweather HMI Active Region Patch (SHARP) cylindrical equal-area (CEA) coordinate continuum intensity maps, SHARP CEA coordinate vector magnetic field maps, and helioprojective-Cartesian coordinate vector magnetic field images, which are observed by Helioseismic and Magnetic Imager (HMI; Scherrer et al. 2012) on board SDO. In this work, we use EUV images with a cadence of 12 s, as well as magnetic field maps and continuum intensity maps with a cadence of 12 min.

2.2. Overview of the CME-flare event

A major CME and its associated X1.4 class flare occurred on July 12, 2012, in the active region National Oceanic and Atmospheric Administration (NOAA) 11520 (see Fig. 1). The Geostationary Operational Environmental Satellite (GOES) soft X-ray flux rapidly increases since ~16:10 universal time (UT) and peaks at ~16:49 UT. This event is thoroughly studied in many works, for example, those focusing on the slipping reconnection related to the formation of the (pre-)eruptive structure (Dudík et al. 2014) or studying the formation of a double-decker flux rope in the source region (Cheng et al. 2014). In the following, we briefly review the evolution of this event and we refer readers to these previous works for more details.

As shown in Figs. 2a–f and Movie 1, the formation of the pre-eruptive structure starts at ~15:00 UT, represented by the appearance of the first bright arcade (marked by the red arrow in Fig. 2a). Afterwards, several bright arcades rapidly develop: their eastern footpoints (pointed by yellow arrows in Figs. 2b,c) quickly slip toward the east, starting from the eastern footpoint of the first bright arcade (marked by the yellow arrow in Fig. 2a) and along the bright ribbons in the negative polarity (visible at the 304 Å passband; see Figs. 2h,i). The details of this process are also exhibited in Figs. 6 and 8 in Dudík et al. (2014). The pre-eruptive structure, appearing as a hot channel at the 131 Å passband (marked by black dashed lines in Figs. 2b,c), is gradually formed at the same time. In this process, the fainter pre-eruptive structure lies above the bright arcades, with its eastern footpoint rooted close to the easternmost footpoints of bright arcades and also slipping along the bright ribbons in the negative polarity. The western footpoint of the hot channel (marked by the orange dashed box in Figs. 2b,c and 3a–d) is mainly anchored in a small adjacent positive sunspot (P'_1 ; see Fig. 3, around $(X, Y) = (50, -365)$ arcsec), close to those of the bright arcades in the main positive sunspot (P_1 ; also see Fig. 3, around $(X, Y) = (40, -335)$ arcsec). The eruption of the

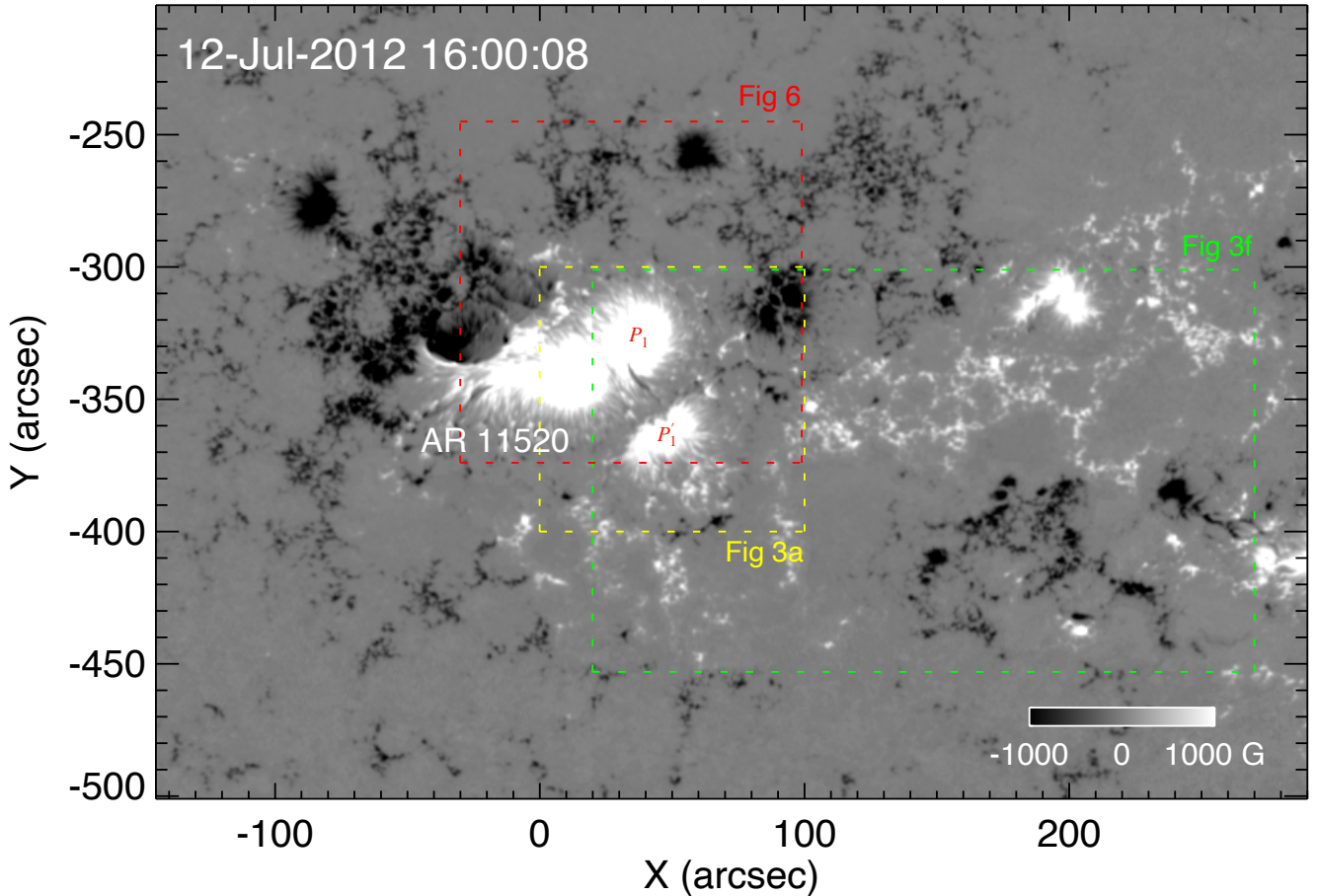


Fig. 1. Vertical magnetic field (B_z , component of magnetic field perpendicular to the solar surface) image of the source region of the CME-flare event on July 12, 2012. The field of view is the same as that in Fig. 2. The yellow, green, and red dashed boxes show the field of view in Figs. 3a, 3f, and 6, respectively. Here, P_1 and P_1' mark the main positive polarity and the adjacent positive polarity, respectively.

hot channel starts at around 16:12 UT (Fig. 2d), and the slipping motion in the negative polarity continues at the onset of and during the eruption (marked by yellow arrows in Figs. 2d,e). The eastern ribbon hook (pointed by the purple arrow in Fig. 2e) represents the eastern CME footprint and develops rapidly during the eruption.

At the AIA 304 Å passband (see Figs. 2g–i and Movie 2), an undisturbed filament appears in this active region during the above whole process. It lies below the pre-eruptive hot channel before the eruption (Figs. 2h,i), while it still stays on the spot and below the post-flare loops during and after the eruption (Figs. 2j–l). This indicates that the eruptive hot channel and the filament are in the upper part and the lower part of a double-decker structure, respectively, in agreement with the views in Cheng et al. (2014). The filament is quite stable and inactive before and during the eruption, unaffected by the formation and eruption of the hot channel.

2.3. Evolution of the western leg of the hot channel

In particular, we focus on the evolution of the western leg of the hot channel. Before the eruption onset, as shown in Figs. 3a–d, some bright loops (see their footpoints pointed by black arrows in Figs. 3c,d) slip along a bright lane (visible at 131 Å and 304 Å passbands; marked by the blue dashed line in Figs. 3a–d), from the western foot of the filament (in the main positive sunspot)

to the western foot of the hot channel (in the adjacent positive sunspot). This slipping motion is also demonstrated in the time-slice plot of the 131 Å intensity along the blue dashed line (Fig. 3e). These suggest that the hot channel loops are originally rooted close to the filament footpoint, while they soon slip to the hot channel footpoint (the orange dashed box) that we see.

Starting at ~15:51 UT (still before the eruption), some loops in the western leg of the hot channel further slip toward west (see their footpoints pointed by black arrows in Figs. 3g–i) along a narrow extended ribbon (pointed by the blue arrow in Fig. 2j) in the western positive-polarity faculae (with X-coordinate in the range of [100,250] arcsec), while the rest part of the western leg is still anchored in the adjacent positive sunspot. After the eruption onset, the bright loops continue to slip along the extended ribbon, the latter of which soon develops into the western ribbon hook (pointed by the blue arrow in Fig. 2k) and represents the western CME footprint. It is ambiguous if previous hot channel footpoints in the adjacent positive sunspot are a part of the CME footprint, as the field lines anchored there are faint during the eruption.

2.4. Properties of the sunspot scar

In the following, we study the source region of the CME-flare event in detail at four moments: 14:58 UT, 16:10 UT, 16:34 UT, and 00:46 UT on July 13, which represent the stage before, at the onset of, during, and after the eruption, respectively. As shown in

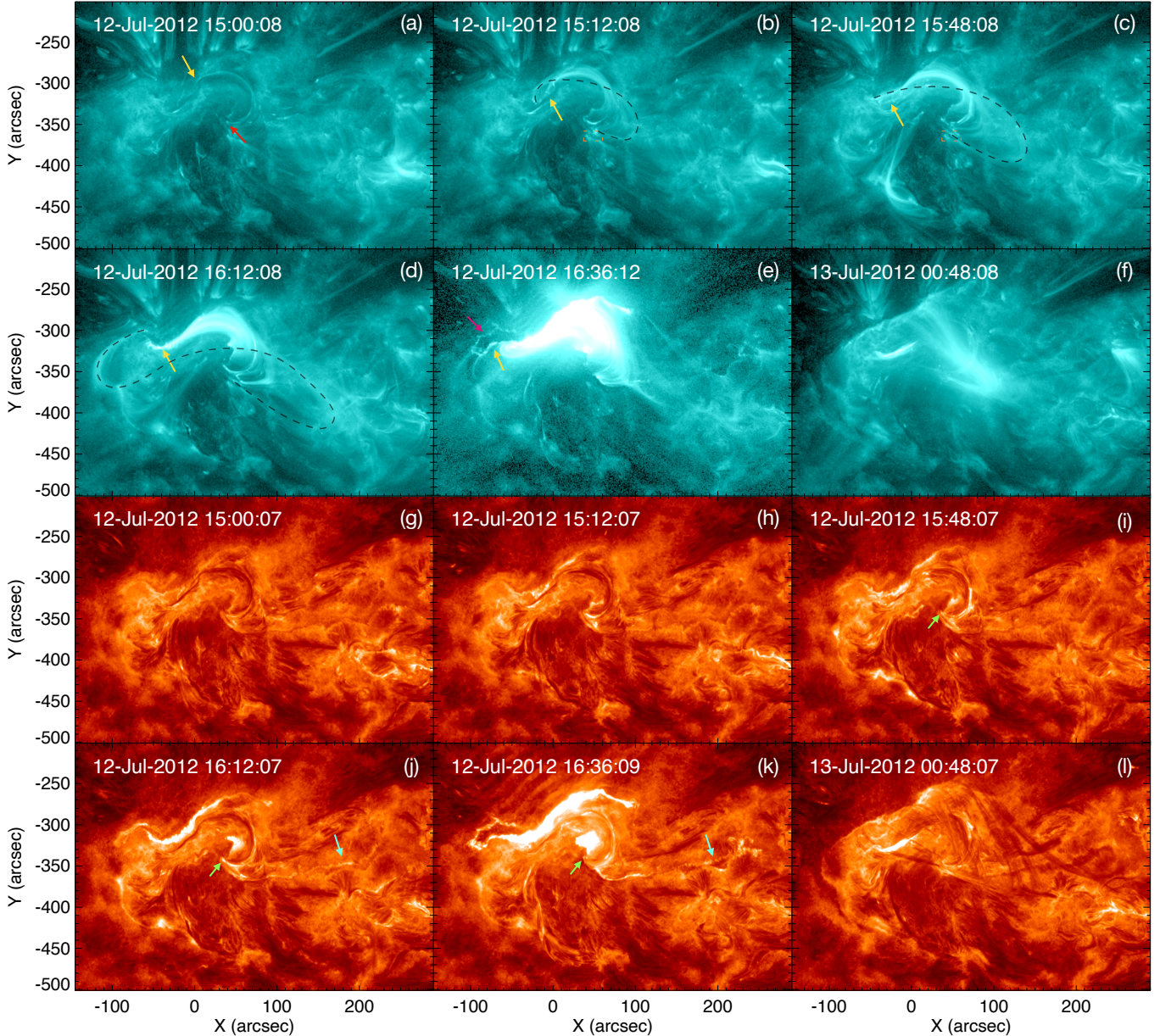


Fig. 2. AIA 131 Å images (panels a–f) and 304 Å images (panels g–l) of the source region of the CME-flare event on July 12, 2012. The red arrow in panel a marks the first bright arcade at 15:00 UT. The yellow arrows in panels a–e mark the slipping motion of the eastern footpoints of the bright arcades in the negative polarity. The dashed lines in panels b–d show the pre-eruptive hot channel. The orange dashed box in panels b and c marks the western footpoint region of the hot channel. The eastern footpoint of the CME is marked by the purple arrow in panel e and the western one is marked by the blue arrow in panel k. The blue arrow in panel j shows the narrow ribbon lane along which the bright loops slip. The green arrows in panels i–k point the western footpoint of the low-lying filament. Two movies of this figure are available [online](#).

Figs. 4a,b, both the main sunspot umbra in the source region and its corresponding positive polarity (around $(X, Y) = (84, -17)$ CEA degree) are composed of two parts.

Since $\sim 13:34$ UT, an arc-shaped structure wedges into the western part of the main positive sunspot (Fig. 4b and Movie 3), which we call a “sunspot scar” throughout the rest of this paper. The sunspot scar appears and continuously drifts toward the south-east both before and after the eruption onset. It shows a significant decrease in the vertical magnetic field strength (B_z ; component of magnetic field perpendicular to the solar surface) as compared to those in the surrounding umbra, while its polarity still remains positive almost everywhere. In Fig. 5b, we show B_z along the orange slit crossing through the sunspot scar (see

the slit in Fig. 4b): B_z is reduced by 39–67% at the center of the sunspot scar at four moments, compared to the average of B_z at two edges of the sunspot scar which are marked by the gray dashed lines in Fig. 5. In the white light passband, the sunspot scar appears as a curved lane of bright materials, which resembles a narrow light bridge, in the western part of the umbra (Fig. 4a and Movie 3). The sunspot scar matches well with this narrow light bridge at the first three moments, as the local dip of B_z in the scar (marked by the black dashed line in Fig. 5b) is co-spatial with the local peak of the continuum intensity in the light bridge (see Fig. 5a). For the fourth moment, we consider that they still match with each other; the mismatch between the local peak of continuum intensity and the local dip of B_z

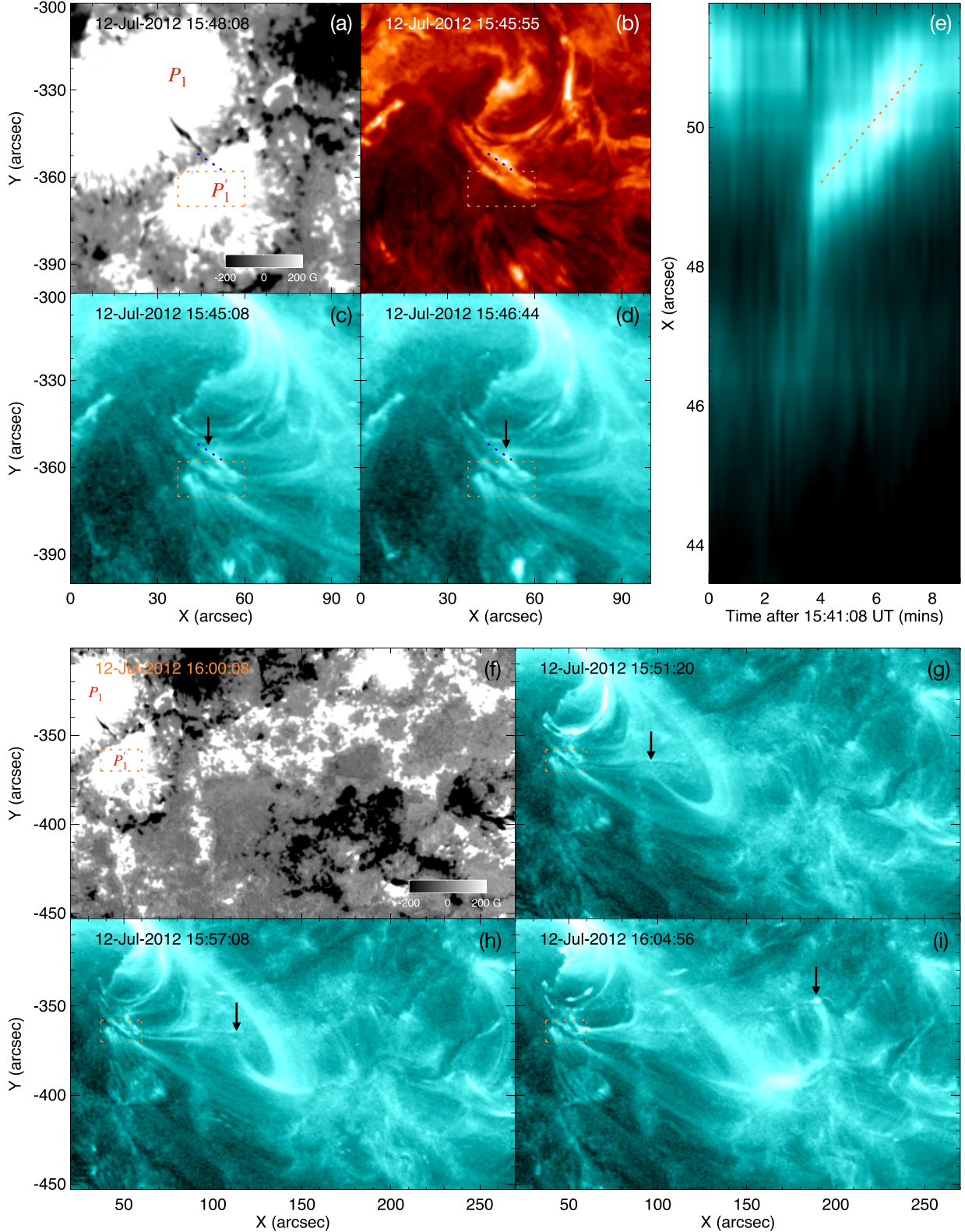


Fig. 3. Slipping motions of loops in the western leg of the hot channel, from the main positive sunspot to the adjacent positive sunspot (panels a–e) and further from the adjacent positive sunspot toward west (panels f–i). (a) Vertical magnetic field image showing the main positive sunspot (P_1) and the adjacent positive sunspot (P'_1). (b) 304 Å image with a same field of view as panel a. (c, d) 131 Å images with a same field of view as panel a. In panels a–d, the orange dashed box marks the western footpoint region of the hot channel, and the blue dashed line represents the bright lane along which the bright loops at the 131 Å passband slip. The black arrows mark the footpoints of the slipping bright loops. (e) Time-slice plot of the 131 Å intensity along the blue dashed line in panels c and d. The orange dashed line in it marks the slipping motion of the bright loop footpoint. (f) Vertical magnetic field image showing the main positive polarity (P_1), the adjacent positive polarity (P'_1), and the western positive-polarity faculae. (g–i) 131 Å images with a same field of view as panel f. The orange dashed box in panels f–i is the same as that in panels a–d. The black arrows mark the footpoints of the slipping bright loops.

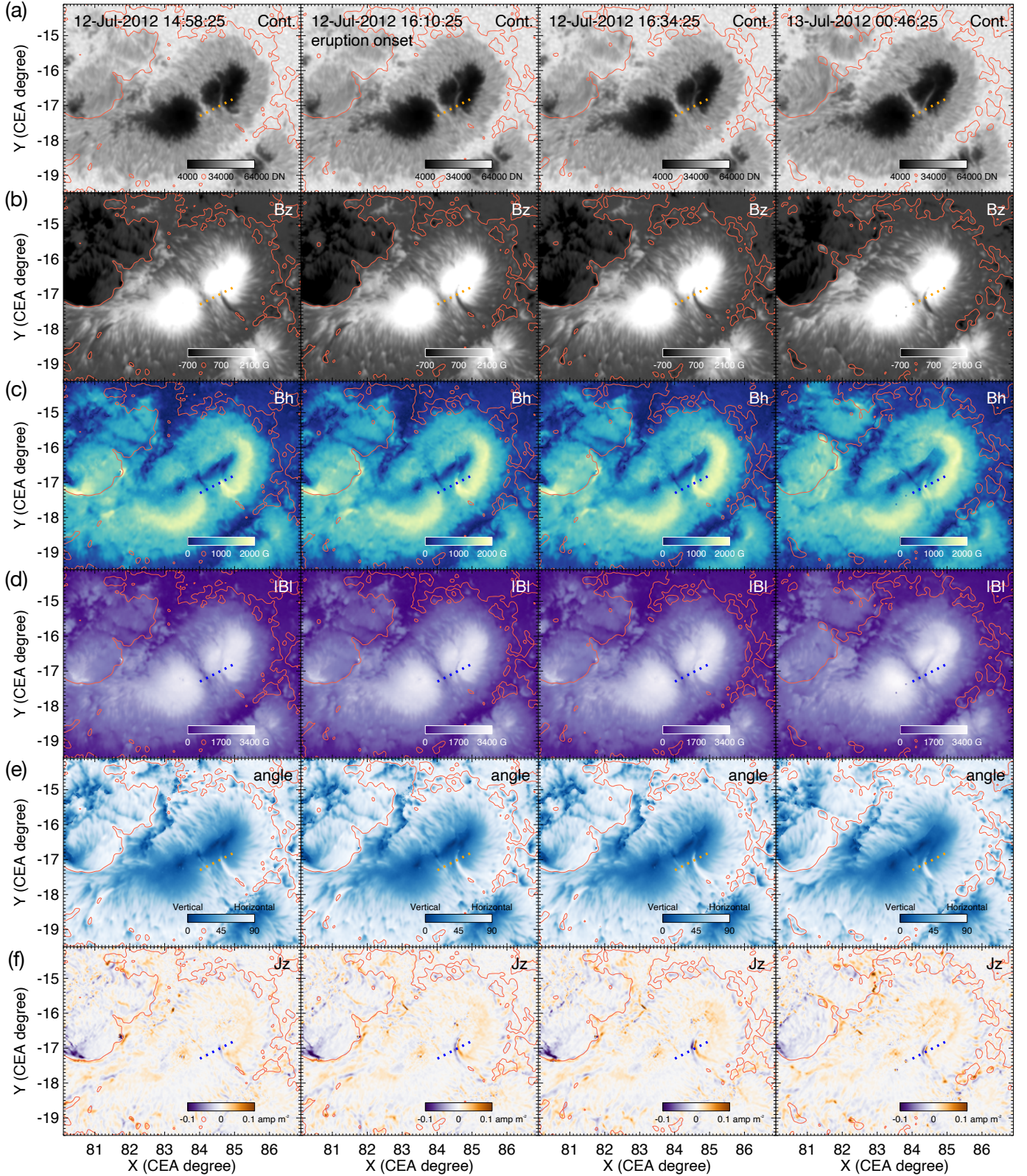


Fig. 4. Continuum intensity (Cont.; panel a), vertical magnetic field strength (B_z ; panel b), horizontal magnetic field strength (B_h ; panel c), total magnetic field strength ($|B|$; panel d), inclination angle of the direction of magnetic field to the vertical direction (angle; panel e), and the vertical current density (J_z ; panel f) images of the source region, which are in SHARP CEA coordinate and at four moments. The time of images in each column is shown in the first row of them. The red contour in each sub-panel shows the PIL. The orange or blue dashed line in each sub-panel is the slit crossing through the sunspot scar, along which the 1D parameters are shown in Fig. 5. A movie of this figure is available [online](#).

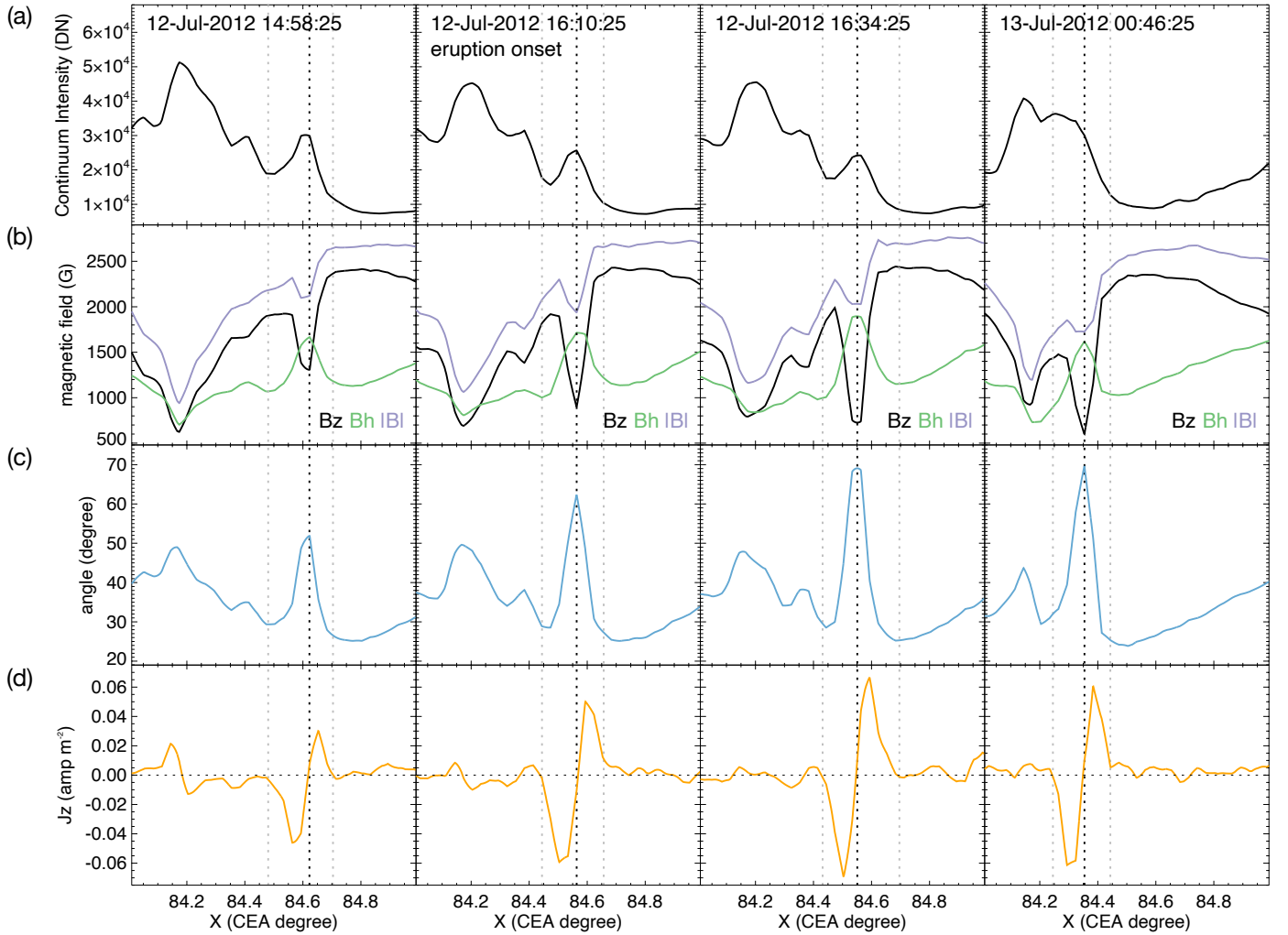


Fig. 5. 1D parameters along the slit crossing through the sunspot scar (dashed lines in Fig. 4). From the top to the bottom, they are continuum intensity (panel a), total magnetic field strength ($|B|$; panel b), vertical magnetic field strength (B_z ; panel b), horizontal magnetic field strength (B_h ; panel b), inclination angle (panel c), and vertical current density (J_z ; panel d). The time of sub-panels in each column is shown in the first row of them. The black vertical dashed line in each column marks the dip of B_z in the sunspot scar, which is regarded as the sunspot scar center. The gray dashed lines in each column show the range of the two peaks in J_z which are at two sides of the sunspot scar, representing the edges of the sunspot scar. The black horizontal dashed line in panel d marks the value where the current density equals zero.

(Figs. 5a,b) is due to that the curved drifting scar-related light bridge merges with the other brighter light bridge which separates the two parts of the umbra (see Fig. 4 and Movie 3). At the center of the sunspot scar, the continuum intensity increases by 72%–95% at the first three moments (see that in Fig. 5a, which is along the orange slit in Fig. 4a).

Furthermore, the sunspot scar also shows marked features in aspect of other parameters of magnetic field at all four moments (see Figs. 4c–f). The details of these parameters, sampled by those along the slit crossing through the sunspot scar (the orange and blue dashed lines in Figs. 4c–f), are exhibited in Figs. 5b–d. In the sunspot scar, there is an obvious enhancement in the horizontal magnetic field strength (B_h ; component of magnetic field parallel to the solar surface; Figs. 4c and 5b). Along the slit, B_h is enhanced by 48–76% at the sunspot scar center at four moments, compared to the average of B_h at the two edges of the sunspot scar. The reduction in B_z and the enhancement of B_h together lead to a more horizontal field, characterized by the larger inclination angle between the magnetic field direction and the vertical direction (Figs. 4e and 5c). At the center of the sunspot scar, the

inclination angle is increased by 24–42 degrees at four moments. The total magnetic field strength ($|B|$) in the sunspot scar is a bit weaker than those in the surrounding umbra (Fig. 4d), with a 12–18% reduction at the scar center at four moments (see Fig. 5b). The vertical current density (J_z) is close to zero at the center of the scar (see Figs. 4f and 5d), however, it has a positive peak on one side of the sunspot scar which the scar curves inward to (hereafter referred to as the “inner side”) and a negative peak on the other side (hereafter referred to as the “outer side”).

We note that the sunspot scar is significantly different from the penumbra, as the above parameters (especially the inclination angle and B_z) are homogeneous in the most part of the former while heterogeneous in the latter. However, we also notice that sometimes the sunspot scar exhibits opposite B_z in a small area at its end close to the penumbra (contoured by the red contours around $(X, Y) = (85, -17.6)$ CEA degree in B_z maps at first three moments in Fig. 4). The formation of this small structure may be due to that the convection in the sunspot scar may become different in the condition of the more horizontal field there and further lead to the formation of small loops locally in

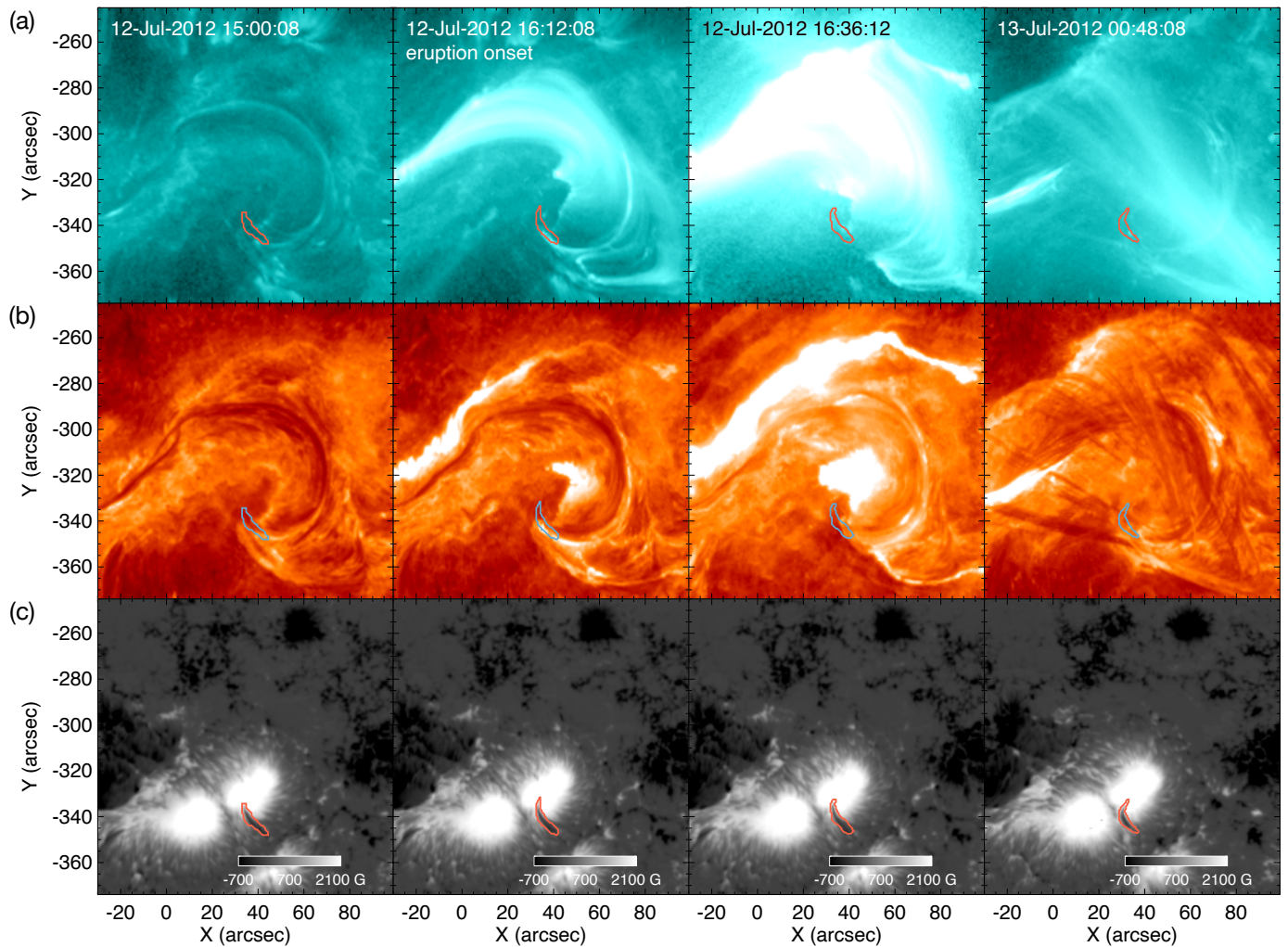


Fig. 6. 131 Å images (panel a), 304 Å images (panel b), and vertical magnetic field images (panel c) of the source region, which are all in helioprojective-Cartesian coordinate and at four moments. The time of images in each column is shown in the first row of them. The red or blue contours in all sub-panels outline the sunspot scar.

the sunspot scar. This possible special convection in the sunspot scar may even be the cause for the narrow light bridge that we observe.

2.5. Possible link between the sunspot scar and the double-decker structure

In Fig. 6, we show EUV images and vertical magnetic field images in helioprojective-Cartesian coordinates, focusing on the sunspot scar. The red (or blue) contour, standing for the outline of the sunspot scar, is overlaid on EUV and B_z images. At the AIA 131 Å passband, we find that there are flickering bright arcades anchored in the sunspot scar, specifically, at the left boundary of the sunspot scar, before and at the onset of the eruption; actually, the bright arcade at 15:00 UT is the first one mentioned in Sect. 2.2. During and after the eruption, due to the overexposure and foreground occlusion, the structures rooted close to the sunspot scar are elusive at the 131 Å passband. In addition, as shown at the AIA 304 Å passband, the western footpoint of the filament is anchored at the inner side of the sunspot scar at all four moments.

As described in Sect. 2.2, the pre-eruptive hot channel appears shortly after the bright arcades appear; it lies above the

bright arcades with its two footpoints being always co-spatial with the two ends of the footpoints of the bright arcades in two polarities. This configuration is quite similar to that in the three-dimensional (3D) standard model for the CME-flare (Aulanier et al. 2012; Janvier et al. 2013, 2014; Aulanier & Dudík 2019), in which the flux rope field lines are formed by the slipping reconnection. In the model, under the slipping reconnection, the field line anchored at a fixed point in one polarity will evolve from an inclined loop first to a highly sheared field line and finally to a twisted flux rope field line, with its other footpoint slipping along the ribbon in the other polarity (see Fig. 16 in Dudík et al. 2014). In the present event, the background coronal loops, bright arcades (those in Figs. 2a–d, as mentioned in Sect. 2.2), and twisted hot channel (see the dashed curve in Fig. 2d) correspond exactly to the inclined loop, highly sheared field line, and twisted flux rope in the model, respectively; the slipping motion along the ribbon in the negative polarity corresponds to that of the soon-to-be flux rope field lines in the model. Therefore, we consider that the bright arcades anchored in the sunspot scar are closely related to the formation of the pre-eruptive hot channel, and even specifically, they represent the highly sheared field lines that will soon evolve into flux rope field lines under the slipping reconnection process. In addition, the filament anchored at the

inner side suggests that the field lines rooted there are most likely twisted flux rope field lines. These results strongly suggest that the sunspot scar is closely related to the western footpoint of the double-decker structure.

3. Sunspot scars in observationally-inspired simulations

3.1. Overviews of modeled CMEs and sunspot scars

In the following, we further study sunspot scars in two magnetohydrodynamic (MHD) simulations that model the formation of pre-eruptive structures and the eruption of CMEs. We first give brief overviews of these two simulations and we also refer to Zuccarello et al. (2015) and Xing et al. (in prep.) for more details. In particular, we note that the parameters in simulations are given in dimensionless units (unless otherwise indicated).

“Simulation 1” is the “Run D2” performed by OHM (Zuccarello et al. 2015), which models the CME eruption by solving zero- β MHD equations. The viscosity and resistivity are considered in this simulation. The equations are solved in dimensionless form and the dimensionless units of the length, time, and magnetic field strength are set to 10 Mm, 67.89 s, and 2.53 G, respectively. It should be mentioned that the set of dimensionless units is for consistency with those of “Simulation 2” (see Appendix A), but any other choice is possible depending on the event to fit. The initial field of the simulation is a potential dipole, and the dimensionless distance between the centers of two polarities is about 2. Mimicking the observations, the initial field is first driven into a highly sheared state by the line-tied shearing flow imposed at the bottom $z = 0$ ($10 t_A \leq t \leq 100 t_A$; t is the dimensionless time, and t_A is the Alfvén time unit). Later, driven by the prescribed line-tied converging flow, a pre-eruptive flux rope of the CME is gradually formed by the magnetic reconnection among sheared arcades, in the framework of the flux-cancellation model ($105 t_A \leq t \leq 164 t_A$). After $t = 164 t_A$, the whole system is relaxed by keeping the bottom boundary stationary; meanwhile, as triggered by the torus instability (TI; Kliem & Török 2006), the flux rope erupts freely as a CME after $t = 164 t_A$.

“Simulation 2” refers to “Simulation Ue” in Xing et al. (in prep.), which studies the CME eruption in a finite- β condition (see Appendix A and Xing et al., in prep. for more details about the numerical setups including dimensionless units and also the kinematics of the flux rope). The simulation is performed by MPI-AMRVAC (Xia et al. 2018), and it solves thermal-MHD equations, which include an internal energy equation and incorporate gravity, viscosity, resistivity, and thermal conduction. The initial condition of the simulation is a combination of a bipolar potential field (where the dimensionless distance between the two polarity centers is also about 2) and a hydrostatic corona with a uniform temperature of 1.6 MK. Similarly to the first simulation, the initial field is first driven into a highly sheared field under the line-tied shearing flow imposed at the bottom $z = 0.015$ ($0 \leq t \leq 18$), then a pre-eruptive flux rope of the CME is formed by the flux cancellation ($18 < t \leq 60$) under the line-tied converging flow, and finally the system is relaxed and the CME erupts after that ($60 < t \leq 71$). Specifically, we note that the modeled flux rope rises almost linearly before $t = 68.5$, while it then rises exponentially afterward, which implies that the onset time of the CME as usually defined in observational analyses (e.g., McCauley et al. 2015; Cheng et al. 2020) is $t = 68.5$ in this simulation.

Aside from the difference in the equations solved, the key differences between the two simulations are the symmetry and the diffusion pattern of the polarities. The dipole in “Simulation 1” is asymmetrical while that in “Simulation 2” is symmetrical. The converging flow in “Simulation 1” diffuses the entire polarities, while the converging flow in “Simulation 2” mainly diffuses the periphery of the polarities (see Figs. 7a,c).

As an overview, in Fig. 7a, we show the snapshot of vertical magnetic field on the plane $z = 0.2$ at $t = 224 t_A$ for “Simulation 1”; similarly, we show that on the plane $z = 0.1$ at $t = 71$ for “Simulation 2” in Fig. 7c. In the following, for “Simulation 1” and “Simulation 2”, we choose to observe the modeled sunspot scars in these two planes which are slightly above the bottom surface, respectively. This choice is due to that the line-tied boundary conditions only allow the vertical magnetic field on the bottom surface to evolve as prescribed by the flows there in the condition of ideal MHD. Since we do not deliberately impose special flows to form the sunspot scar on the bottom surface, no sunspot scar can be present in this line-tied plane. Therefore, we choose an altitude slightly above the bottom: on the one hand, the magnetic field is free to evolve at this altitude under the combined constraints of the underlying line-tying and the overlaying coronal evolution; on the other hand, this altitude above the line-tied plane is sufficiently low to be considered at the bottom of the corona, close enough to the photosphere. We then fine-tuned the choice of these altitudes between the bottom and $z = 0.2$ for both two simulations to allow for the best visibility of the scars, within the limits of our models. In addition, this choice means that, when we compare observations with simulations in the following, we implicitly assume that in observations, the photospheric altitude that corresponds to that of HMI observations is located above the solar depth at which the line-tying is at work.

It is clear that there are sunspot scars in both the positive and the negative polarities for these two simulations, regardless of whether the bipolar field is symmetrical or not and how the active region is diffused. For each sunspot scar in each simulation, a bunch of field lines are traced from a rake crossing through it. As shown in panels b and d, some of magnetic field lines are CME flux rope field lines (green tubes) while some others correspond to surrounding inclined loops (magenta tubes). In the following, we will study the magnetic properties of sunspot scars mainly through “Simulation 1”, considering that its sunspot scars are more similar to that in observations; we also study the thermal properties of sunspot scars through “Simulation 2”, benefiting from the thermal-MHD equations it solves.

3.2. Properties of modeled sunspot scars

We first studied the properties of the modeled sunspot scar in the positive polarity on the plane $z = 0.2$ of “Simulation 1” at three moments ($144 t_A$, $164 t_A$, and $184 t_A$, which are before, at, and after the torus instability onset, respectively). As shown in Fig. 8 and Movie 4, the sunspot scar appears and continuously drifts both before and during the eruption, similar to what is seen in observations. We also set a slit crossing through the sunspot scar (marked by the orange and blue dashed lines in Fig. 8), the detailed properties of the sunspot scar along which are exhibited in Fig. 9. Obviously, the vertical magnetic field strength is weaker in the sunspot scar (Figs. 8a and 9b). It is also clear that there is a stronger horizontal magnetic field (Figs. 8b and 9b) and a larger inclination angle (Figs. 8c and 9c) in the sunspot scar. The vertical current density is close to zero at the center of the sunspot scar and has a positive peak at the inner side of the

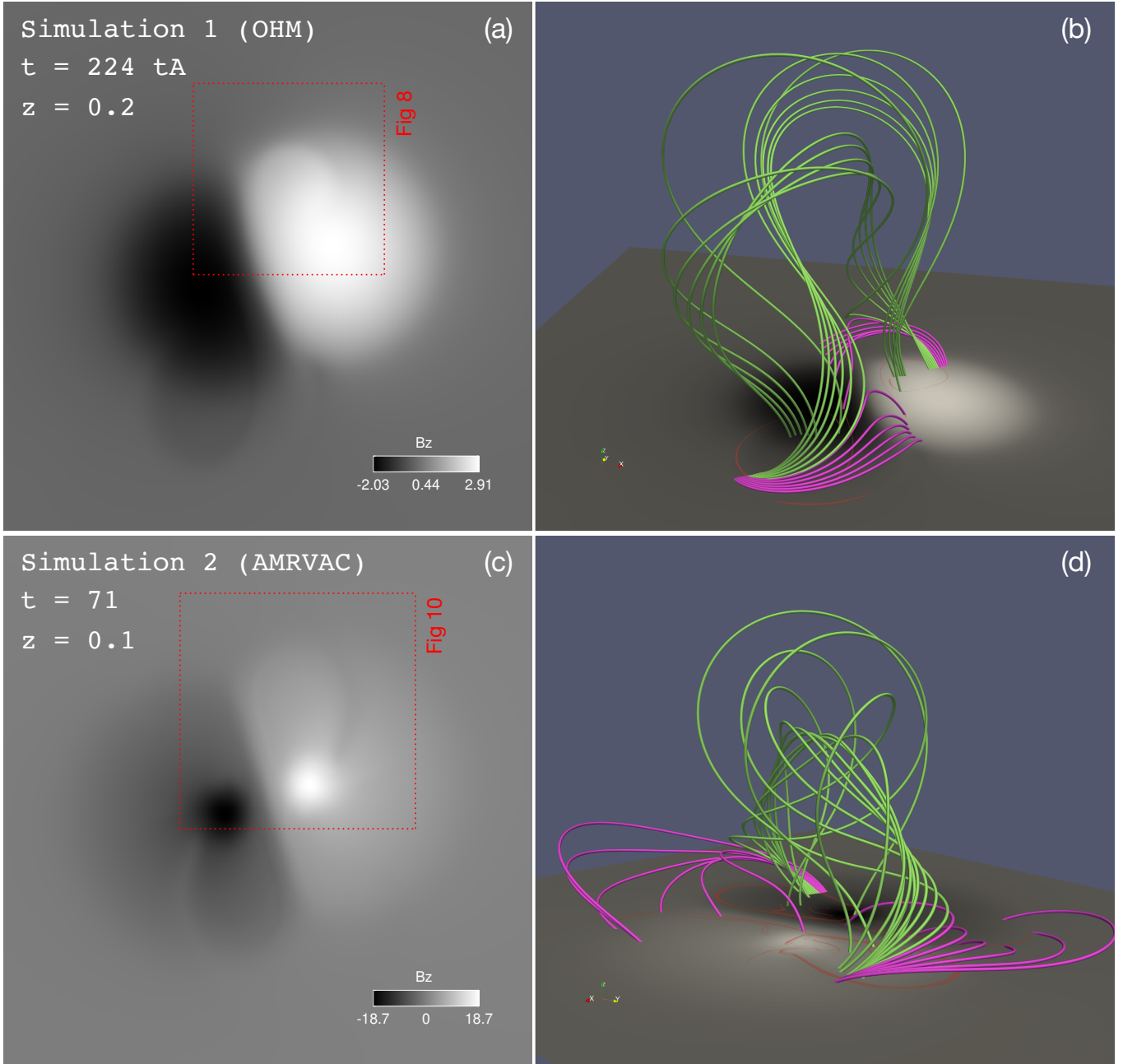


Fig. 7. Snapshots of sunspot scars and the field lines traced from rakes crossing through sunspot scars for both “Simulation 1” and “Simulation 2”. (a) Snapshot of vertical magnetic field on the plane $z = 0.2$ at $t = 224 t_A$ in “Simulation 1”. The red dashed box shows the field of view in Fig. 8. (b) Magnetic field lines traced from two rakes at $t = 224 t_A$ which cross through the two sunspot scars in the two polarities, respectively. The green tubes represent the CME flux rope field lines and the magenta tubes represent the inclined loops. The bottom plane shows the vertical magnetic field on the plane $z = 0.2$, same as that in panel a. The red filled contours show the footprints of QSLs ($\log Q \geq 3$) on this plane. (c) Snapshot of vertical magnetic field on the plane $z = 0.1$ at $t = 71$ in “Simulation 2”. The red dashed box shows the field of view in Fig. 10. (d) Similar to panel b, but for that at $t = 71$ in “Simulation 2”. The bottom plane shows the vertical magnetic field on the plane $z = 0.1$, same as that in panel c. The green tubes, magenta tubes, and red filled contours have the same meanings as those in panel b.

sunspot scar and a negative peak at the outer side (Figs. 8d and 9d). In addition, we also find that the total current density is also close to zero at the center of the sunspot scar (Fig. 9d).

We further studied the properties of the sunspot scar in “Simulation 2”. In Fig. 10, we show the sunspot scar in the positive polarity on the plane $z = 0.1$, along with detailed information on the sunspot scar along a slit crossing through it (marked by

orange or blue dashed lines in Fig. 10). As shown in Fig. 10 and Movie 5, first, the sunspot scar also has a weaker vertical magnetic field, a stronger horizontal magnetic field, and, thus, a larger inclination angle; second, the vertical and total current densities are also close to zero at the center of the sunspot scar, and the vertical current density has a positive and negative peak at the inner and outer side, respectively. In addition,

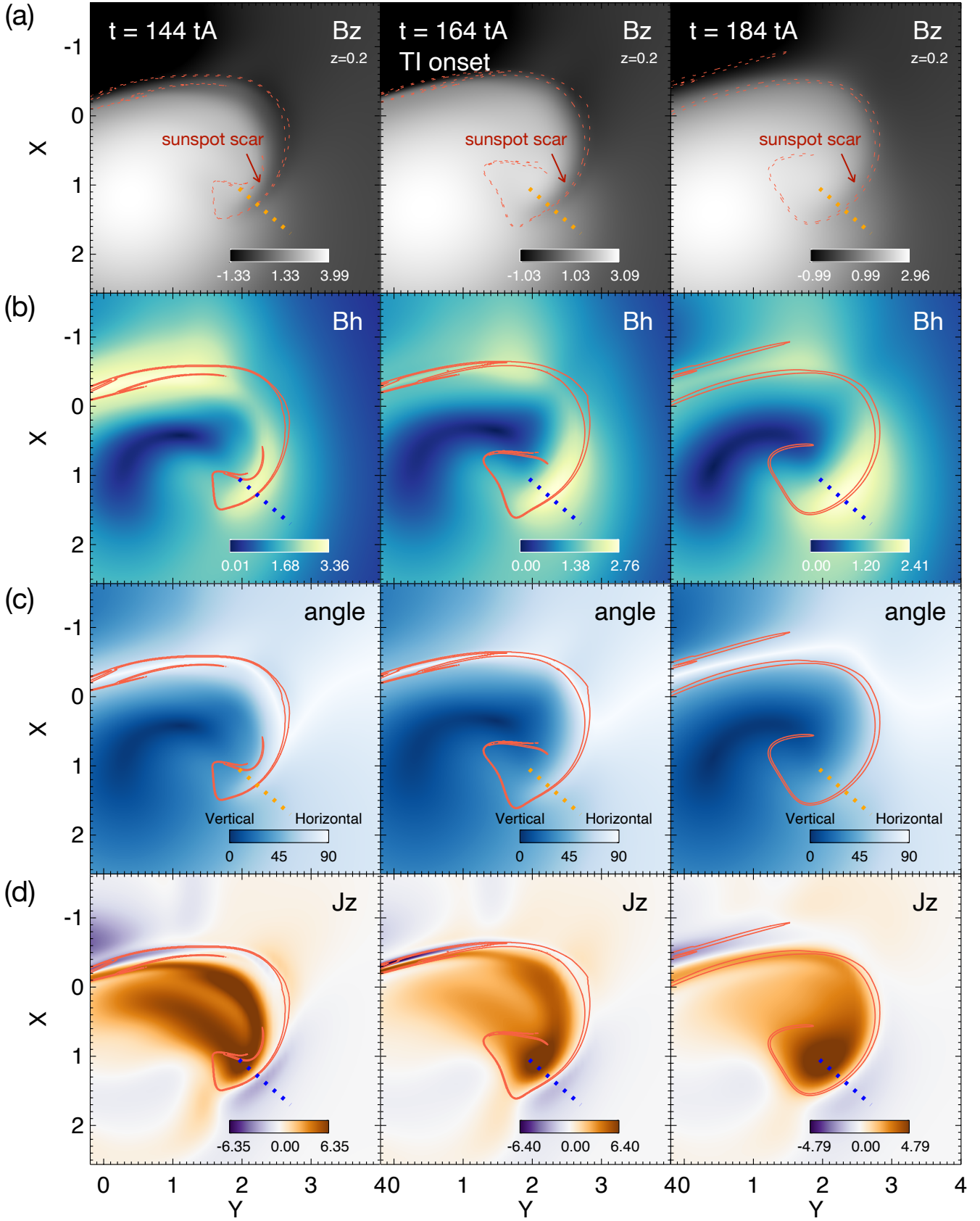


Fig. 8. Distributions of vertical magnetic field strength (B_z ; panel a), horizontal magnetic field strength (B_h ; panel b), inclination angle (angle; panel c), and vertical current density (J_z ; panel d) on the plane $z = 0.2$ at $t = 144 t_A$ (first column), $t = 164 t_A$ (second column), and $t = 184 t_A$ (third column) in “Simulation 1”. The red dashed or solid contour in each sub-panel shows the outline of the footprint of QSLs in this plane, in which $\log Q \geq 3$. The orange or blue dashed line in each sub-panel marks the slit crossing through the sunspot scar, whose 1D plots are shown in Fig. 9. A movie of this figure is available [online](#).

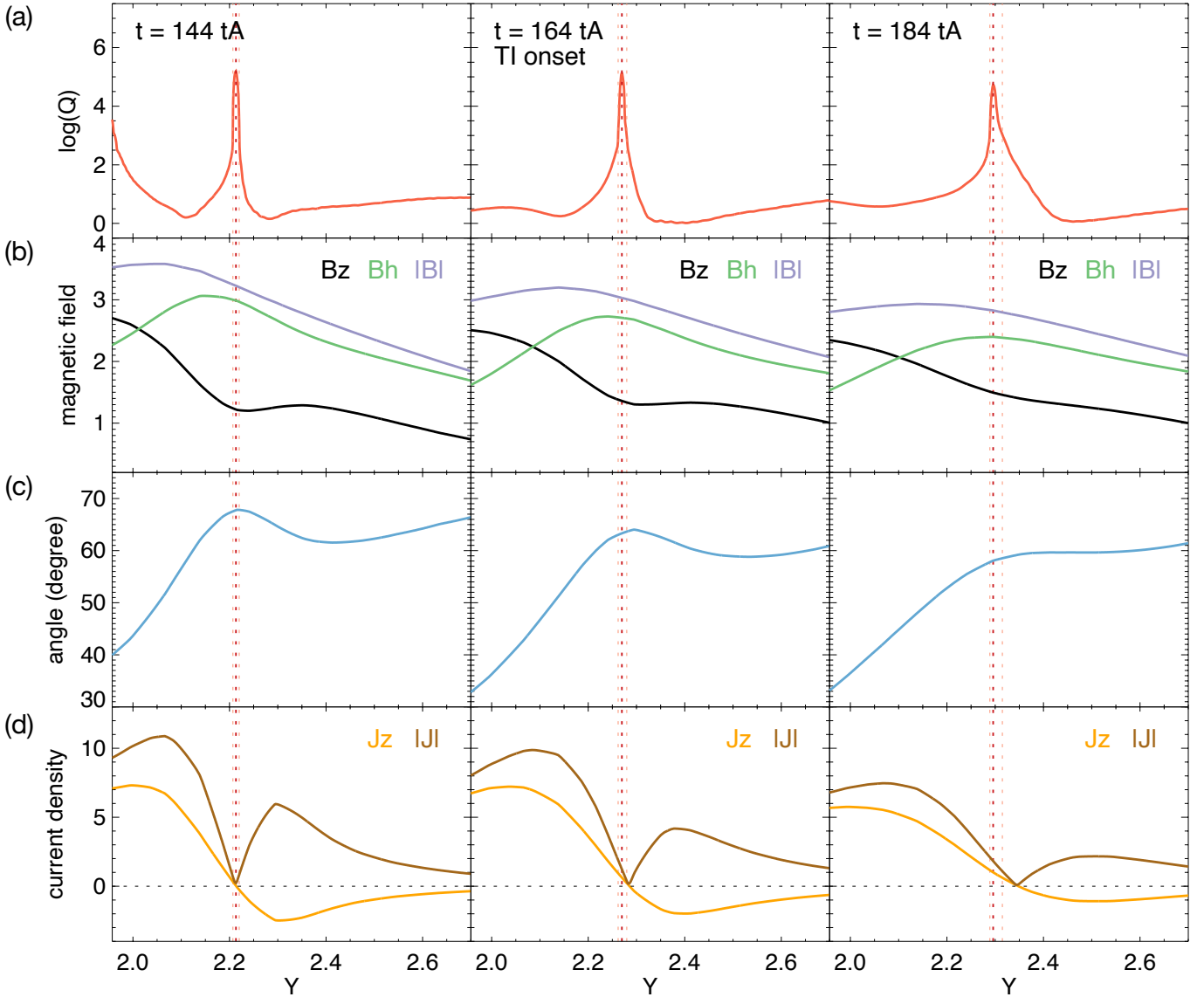


Fig. 9. Profiles of 1D parameters along the slit (dashed lines in Fig. 8) crossing through the sunspot scar at $t = 144 t_A$ (first column), $t = 164 t_A$ (second column), and $t = 184 t_A$ (third column) in “Simulation 1”. From the top to the bottom, they are squashing degree ($\log Q$; panel a), total magnetic field strength ($|B|$; panel b), horizontal magnetic field strength (B_h ; panel b), vertical magnetic field strength (B_z ; panel b), inclination angle (panel c), total current density ($|J|$; panel d), and vertical current density (J_z ; panel d). The red dashed line in each column marks the peak of $\log Q$. The pink dashed lines in each column show the range of the QSL footprint ($\log Q \geq 3$). The black horizontal dashed line in panel d marks the value where the current density equals zero.

the temperature at the inner side of the sunspot scar is 0.16 (0.25 MK in dimensional unit) larger than that at the outer side, while the mass density shows a lane of peak at the outer side of the sunspot scar.

We note that the above features of vertical and horizontal magnetic field strength, inclination angle, and vertical current density in both two simulations are in remarkable agreement with the observations, even though these simulations were merely designed for CME onset and certainly not to fit the sunspot scar a priori.

3.3. Nature of the sunspot scar: Flux rope footprint edge

To explore the nature of the sunspot scar, we further study the squashing degree, Q , which measures the mapping of the field lines, on the plane $z = 0.2$ for “Simulation 1” and on the plane

$z = 0.1$ for “Simulation 2”. The squashing degree is calculated by (Titov et al. 2002):

$$Q = \frac{\left(\frac{\partial X}{\partial x}\right)^2 + \left(\frac{\partial X}{\partial y}\right)^2 + \left(\frac{\partial Y}{\partial x}\right)^2 + \left(\frac{\partial Y}{\partial y}\right)^2}{\left|\frac{\partial X}{\partial x} \frac{\partial Y}{\partial y} - \frac{\partial X}{\partial y} \frac{\partial Y}{\partial x}\right|}, \quad (1)$$

in which (x, y) and (X, Y) are coordinates of two footpoints of a field line. As exhibited in Figs. 8 and 10, the red (or green) dashed (or solid) contour of $\log Q = 3$ shows the outline of the footprint of QSLs, in which the connectivity of field lines varies sharply in space. In Figs. 9a and 10, we also show $\log Q$ along the slit crossing through the sunspot scar, for “Simulation 1” and “Simulation 2”, respectively. For “Simulation 1”, Figs. 8 and 9 clearly show that a section of the hooked part of the QSL footprint matches well and drifts equally with the sunspot scar at

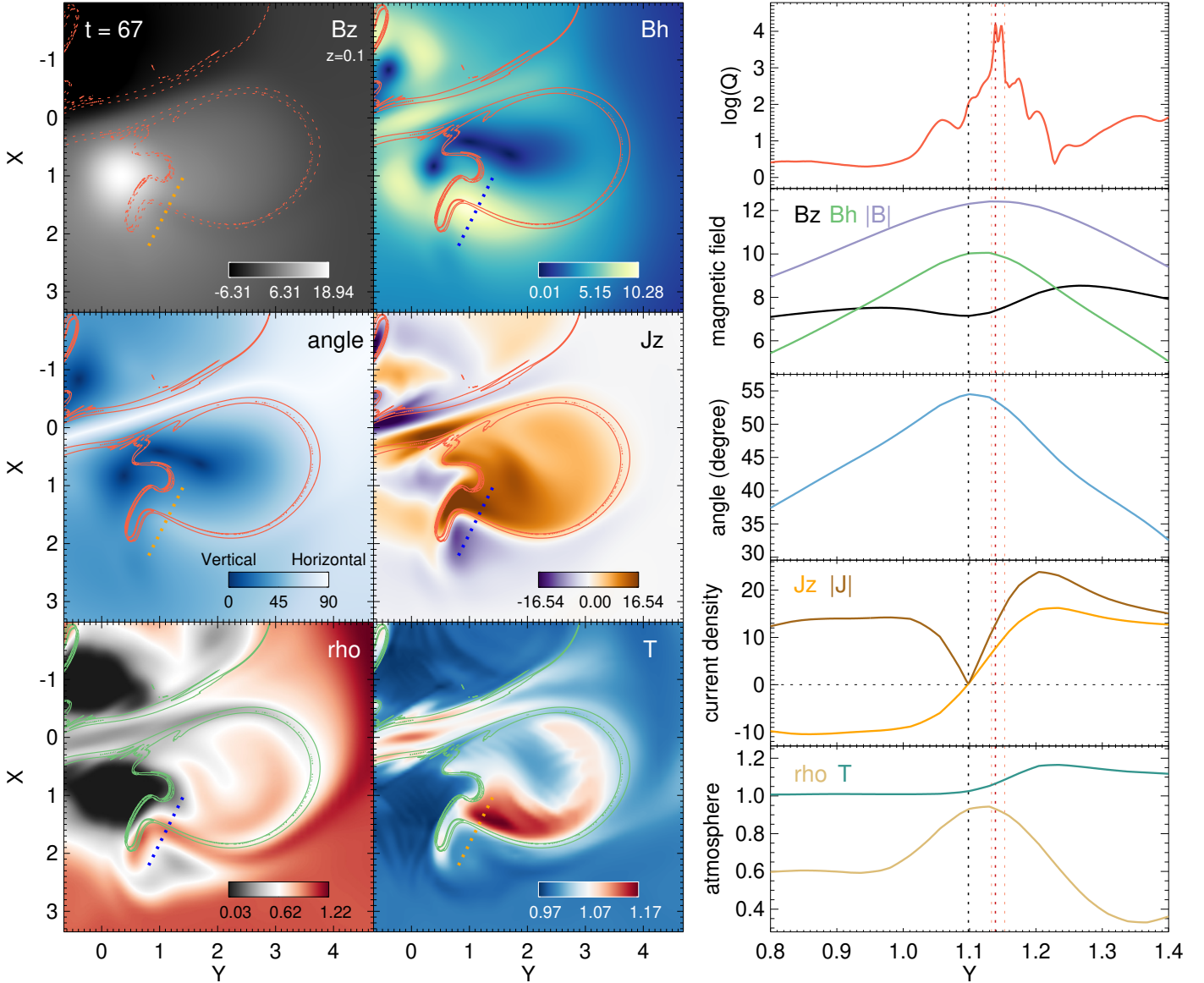


Fig. 10. Properties of the sunspot scar in the positive polarity of “Simulation 2”, shown by the 2D images (left half) and 1D plots of slit crossing through the scar (right half). Left half: Distributions of vertical magnetic field strength (B_z), horizontal magnetic field strength (B_h), inclination angle (angle), vertical current density (J_z), mass density (ρ), and temperature (T) on the plane $z = 0.1$ at $t = 67$ in “Simulation 2.” The red (or green) solid (or dashed) contours outline the QSL footprints on this plane. Right half: 1D plots along the slit crossing through the sunspot scar at $t = 67$ (orange and blue dashed lines in the left half). From the top to the bottom, they are squashing degree ($\log Q$), total magnetic field strength ($|B|$), horizontal magnetic field strength (B_h), vertical magnetic field strength (B_z), inclination angle, total current density ($|J|$), vertical current density (J_z), temperature (T), and mass density (ρ). The red dashed line shows the peak of $\log Q$, and the pink dashed lines demonstrate the range of the QSL footprint ($\log Q \geq 3$). The black vertical dashed line marks the dip of B_z in the sunspot scar. The black horizontal dashed line in the fourth row marks the value where the current density equals zero. A movie of this figure is available [online](#).

all three moments. The similar result for “Simulation 2”, which demonstrates that the sunspot scar is co-spatial with a section of the hooked part of the QSL footprint, is shown in Fig. 10.

In addition, in Fig. 11, we exhibit field lines traced from points along a slit (which is along the slit in Fig. 8) crossing through the sunspot scar in “Simulation 1”. It is clear that the field lines traced from points at the inner side of both the QSL footprint and the sunspot scar are flux rope field lines (blue tubes), while those traced from the other side are inclined loops (yellow tubes). The field lines traced from points in the sunspot scar (green tubes), with their other footpoints anchored on the QSL footprint in the negative polarity, mark the transition between the above two bunches of field lines. Similar results for

“Simulation 2” are shown in Figs. 12a–c, in which the field lines are also traced from points along a slit which crosses through the scar along the slit in Fig. 10. The field lines traced from points at the inner side of, at the outer side of, and within the sunspot scar are also flux rope field lines (blue tubes), inclined loops (yellow tubes), and the transition between the previous two (green tubes), respectively.

In short summary, the above results (about QSL footprints and field lines) strongly indicate that the sunspot scar marks the edge of the footpoint of the flux rope both before and during the eruption, in agreement with our implication in observations that the sunspot scar is closely related to the flux rope footpoint of the double-decker structure.

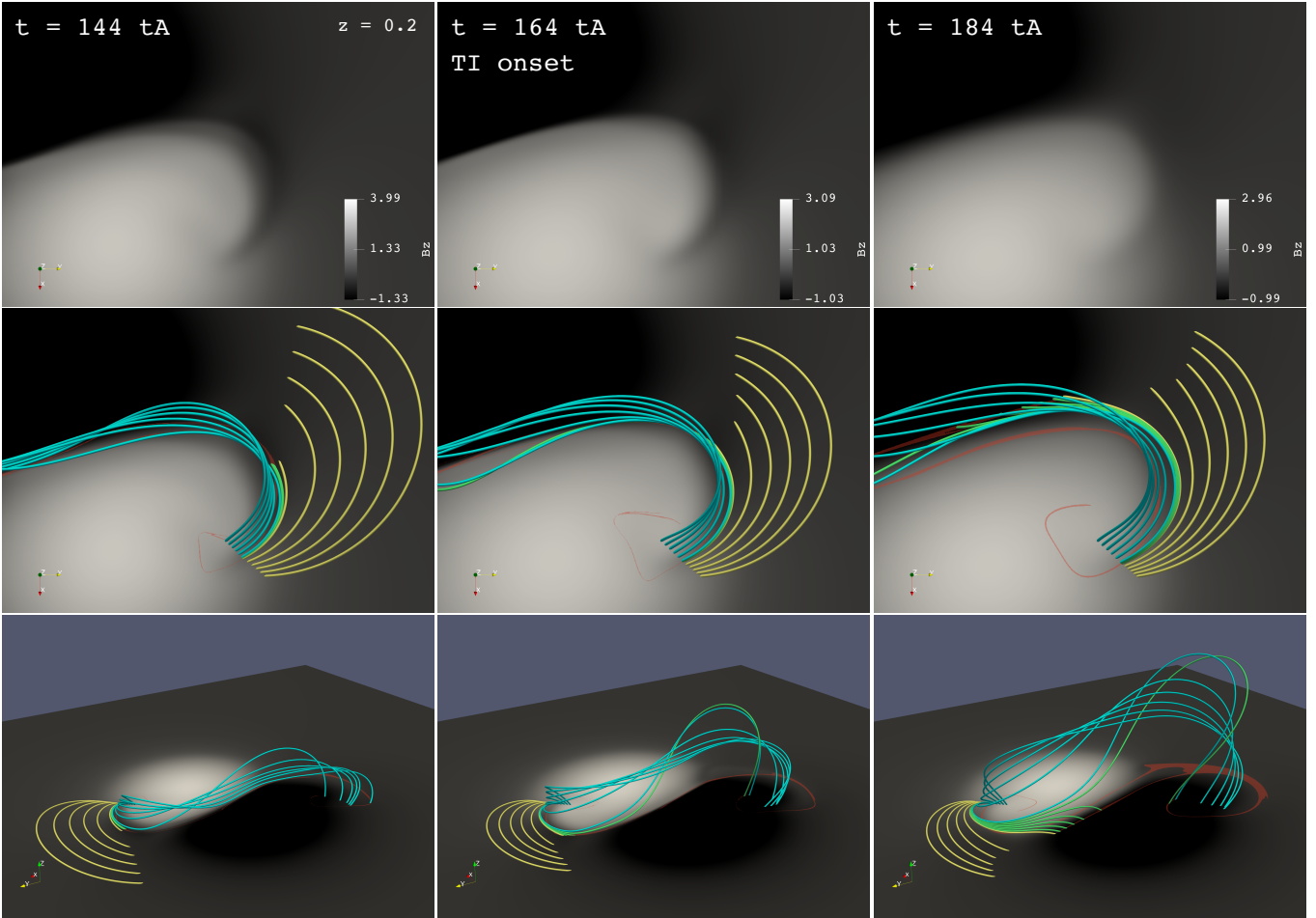


Fig. 11. Snapshots of sunspot scars and the field lines traced from points along a slit crossing through the sunspot scar in the positive polarity at $t = 144 t_A$ (first column), $t = 164 t_A$ (second column), and $t = 184 t_A$ (third column) in “Simulation 1.” The bottom plane in each sub-panel shows the vertical magnetic field on the plane $z = 0.2$, clearly exhibiting the sunspot scar in the positive polarity. The tubes in the second row represent the field lines traced from points on a slit which is along the slit in Fig. 8. The blue tubes represent the flux rope field lines anchored at the inner side of the sunspot scar, the yellow tubes represent the inclined loops anchored at the outer side, and the green tubes represent the field lines which are anchored in the scar and at the transition between the previous two bunches of field lines. The red filled contours show the QSLs footprints on the plane $z = 0.2$. The third row is the oblique view of the second row.

Furthermore, as a thermal-MHD simulation, “Simulation 2” unveils more thermal properties of the field lines anchored in the sunspot scar. The tube in Fig. 12 (shown in panels d–f; the same as the purple tube in panels a–c) reveals the temporal evolution in thermodynamics of a field line rooted inside the sunspot scar. This field line is traced from a fixed point in the positive polarity at the bottom surface ($z = 0.015$), where the velocity is zero during $66 \leq t \leq 68$; this ensures that the footpoint of this field line at the fixed point hardly moves. From $t = 66$ to $t = 68$, this field line crosses through the sunspot scar on the plane $z = 0.1$ with the intersection on the slit. In this period, it evolves from an inclined loop to a highly sheared field line and finally to a flux rope field line, with its footpoint in the negative polarity slipping along the QSL footprints (see Figs. 12a–c). Meanwhile, its temperature increases over time with the maximum temperature along the field line increasing by 0.12 (0.20 MK in dimensional unit) from $t = 66$ to $t = 68$ (see Figs. 12d–f). These results indicate that this field line experiences a slipping reconnection and it is heated by the reconnection, when it is anchored in the sunspot scar.

Especially, we note that the evolution of the tube in Figs. 12d–f is highly consistent with the evolution of the bright arcades and hot channel in observations (see Figs. 2a–d). The modeled field line (bright arcade in observations) is a less hot (less bright) inclined loop at the beginning. Afterwards, it experiences the reconnection, with one of its footpoints slipping along the QSL footprint (bright ribbon); meanwhile, it becomes hotter (brighter) as being heated during the reconnection. Finally, it evolves into a flux rope field line (hot channel thread) when its footpoint slips to the flux rope footpoint (ribbon hook).

As a summary, we conclude that on the one hand, the field lines rooted in the sunspot scar spatially represent the transition between the flux rope and the inclined loops at each moment; on the other hand, the temporal evolution of each field line in the sunspot scar shows the transformation from the inclined loops to the flux rope under the slipping reconnection over time.

Finally, it is worth discussing the temperature of the flux rope and related heating processes in “Simulation 2”. As described in Sects. 3.2 and 3.3, the flux rope (field line) is obviously hotter than the coronal loops, but the temperature difference between

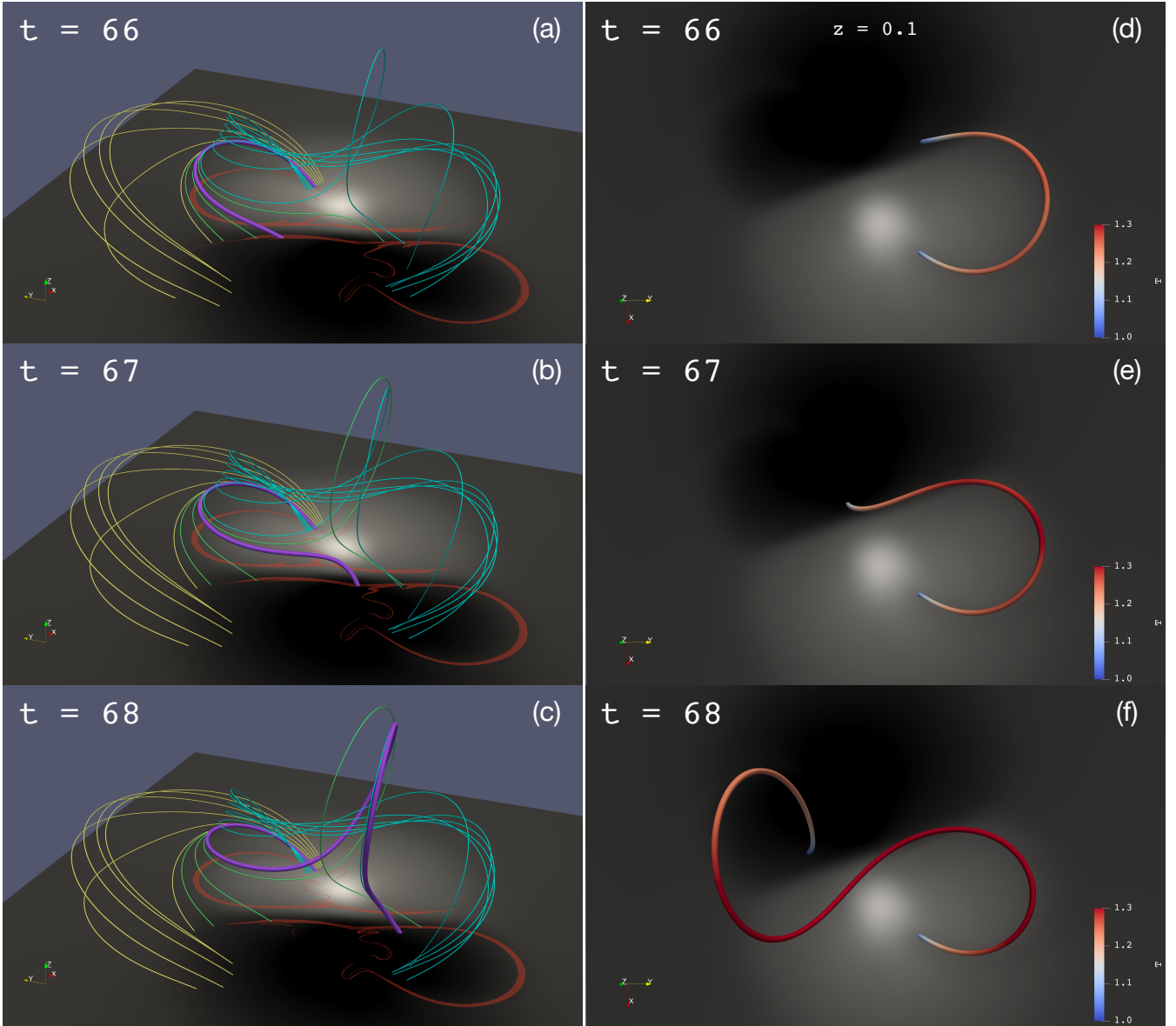


Fig. 12. Snapshots of field lines traced from points on a slit crossing through the sunspot scar in the positive polarity during $66 \leq t \leq 68$ in “Simulation 2”. The bottom plane in each sub-panel exhibits the vertical magnetic field strength on the plane $z = 0.1$. In panels a–c, the thin yellow, green and blue tubes represent the field lines traced from points on a slit which is along the slit in Fig. 10; the thick purple tube represents the field line which is traced from a fixed point at the bottom plane ($z = 0.015$) and crosses through the plane $z = 0.1$ with the intersection in the sunspot scar and on the slit. The red filled contours show the QSLs footprints on the plane $z = 0.1$. Panels d–f show the top view of panels a–c, with only the plane $z = 0.1$ and the thick tube (same as the purple tube in panels a–c) exhibited. The color of the tube shows the temperature along the field line.

these two is not large. This is due to that the maximum magnetic field strength in “Simulation 2” is only about 110 G, quite less than that in observations, which leads to insufficient Ohmic heating during the formation of the modeled flux rope. In addition, the setting of uniform resistivity in the simulation may underestimate the resistivity in the reconnection region, which could also result in the flux rope (field line) not being heated as much as that in observations.

3.4. Explanations of the sunspot scar in the observational event

Considering the high agreement of our simulations with the observations, we explain the relationship between the sunspot scar and the double-decker structure in the observational event

on July 12, 2012, with reference to the nature of the sunspot scar as summarized from our simulations.

Before the eruption onset, the sunspot scar drifts toward the south-east and sweeps over the coronal loop regions. In this process, the coronal loops are successively involved in the slipping reconnection, with their footpoints in the positive polarity relatively passing from the outer side of the sunspot scar to its inner side. During the reconnection, these loops are transformed to highly sheared field lines and meanwhile get heated, appearing as the bright arcades anchored in the sunspot scar; they completely evolve into flux rope field lines when they are anchored at the inner side.

Furthermore, under an extra slipping reconnection, these flux rope field lines slip from the filament footpoint region to the hot channel footpoint region, along a lane connecting the end of the

sunspot scar in the main positive sunspot and the adjacent positive sunspot (see Fig. 3a), after which they appear as loops in the hot channel.

Therefore, we infer that the sunspot scar represents the edge of the footpoint of the pre-eruptive hot channel in observations, which is in agreement with the results in simulations, although the hot channel field lines which are formed in the sunspot scar soon slip to the adjacent sunspot under further reconnection due to the particular complex flux distribution in this non-bipolar active region (see Sect. 2.3).

During and after the eruption, it is unclear to determine the relation between the sunspot scar and the eruptive hot channel, due to the foreground occlusion and the further slipping motion along the western faculae. We may suspect that the reconnection is still ongoing in the sunspot scar as the scar still continuously drifts in this period. The low-lying filament-related flux rope may also contribute to the sunspot scar.

Finally, we note that both the hot channel and the filament in observations and the flux ropes in simulations are forward-S with a right-handed chirality. Therefore, the direct current along the flux rope field line should be in the same sign with the magnetic field, that is, positive in the positive polarity; the return current, which shields the flux rope from the background field, should be antiparallel with the magnetic field, that is, negative in the positive polarity (see Table 1 in Schmieder & Aulanier 2018). The results in observations and simulations are exactly consistent with this definition: in observations, the vertical current density at the inner and outer side of the sunspot scar which is inside and outside the flux rope footpoint is positive and negative, respectively (see Figs. 4f and 5d); similar results, in agreement with the observations, are also shown in simulations (see Figs. 8d and 9d for “Simulation 1” and Fig. 10 for “Simulation 2”).

3.5. Mismatches between observations and simulations

Beyond the above agreement, the observations and simulations still reveal a few inconsistencies. First, B_z , B_h , inclination angle, and J_z in the sunspot scar become more and more inconspicuous over time in “Simulation 1” (see Figs. 9b–d). This implies that the modeled sunspot scar is fading away from before to during the eruption, which does not occur in observations. We infer this difference may be due to that the resistivity in the simulation, which is obviously larger than that in the Sun, may cause the boundary between eruptive vertical field lines and non-eruptive inclined loops to become overly diffuse, thereby both flattening and widening the sunspot scar. The flattening effect indeed smooths the dip and peak of magnetic field and current in the sunspot scar, while the widening effect makes the sunspot scar less visually obvious. This inference is strongly supported by the accelerating fading of the sunspot scar in “Simulation 1” after $t = 164$ (see Movie 4), during which the resistivity is further increased to ensure the stability of the code (see setups in Sect. 2.3 in Zuccarello et al. 2015). In addition, we note that on the one hand, the fading of the sunspot scar directly results from the over-dissipation of the magnetic field in it; on the other hand, the over-dissipation of the magnetic field in regions above the sunspot scar also affects the sunspot scar indirectly by Alfvén waves. Lastly, this mismatch might also be due to that the surviving low-lying filament-related flux rope may also contribute to the sunspot scar in the observation while the low-lying structure (see Fig. 2a in Aulanier & Dudík 2019) does not play such a role in the simulation.

Second, the total magnetic field strength does not show a dip in the modeled sunspot scars at any moments (Figs. 9b and 10),

which is different from that in observations. We speculate that it is also the excessive resistive dissipation in the simulation that erases this feature, especially considering the total magnetic field strength is only reduced a bit in the observational sunspot scar.

In particular, taking the sunspot scar at $t = 144 t_A$ in “Simulation 1” as an example, although B_z at its center is decreased by about 30–40%, its reduction of B_z is still less visually obvious than that at 14:58 UT in observations (see first column of Fig. 5b; B_z is also decreased by 39% at the center of the scar). We point out that this visual effect may be due to the widening of the modeled sunspot scar. The wide dip of B_z in the simulation may result from not only the over-dissipation mentioned above, but also that the spatial resolution of the simulation limits the minimum width of the modeled sunspot scar.

4. Summary

The properties and the nature of the sunspot scar are summarized as a sketch in Fig. 13:

1. Before and during the flux rope eruption, the sunspot scar is manifested as an arc-shaped structure intruding in the positive or negative polarity and appears as a light bridge in the white light passband. The magnetic field in the sunspot scar is more inclined with a stronger horizontal magnetic field and a weaker vertical magnetic field relative to those at the surrounding umbra. In addition, the sunspot scar is more homogeneous than the surrounding penumbra, in the latter of which the distributions of inclination angle and B_z are intercombed. Both the vertical current density and the total current density are close to zero at the center of the sunspot scar, while they both have two peaks at two sides;
2. Spatially, the sunspot scar represents the edge of the flux rope footpoint. The sunspot scar matches well with a section of the hooked part of QSL footprints. At the inner side of the sunspot scar, the magnetic field lines are flux rope field lines and carry a parallel direct current (DC) in condition of a forward-S flux rope; while, at the outer side, the field lines are coronal loops where the return current (RC) is antiparallel to the magnetic field in the same condition. The field lines rooted in the sunspot scar are highly sheared, as a spatial transition between the previous two bunches of field lines;
3. Temporally, the sunspot scar continuously drifts before and during the eruption, showing the drifting and the deformation of the flux rope footpoint (Aulanier & Dudík 2019; Lörinčík et al. 2019; Xing et al. 2020; Gou et al. 2023). As an area that was originally at the outer side is swept by the sunspot scar and is brought to the inner side, the field lines anchored there experience a slipping reconnection with their footpoints in the other polarity slipping along the QSL footprint. In this process, these field lines evolve from the background coronal loops to highly sheared field lines and, finally, to the flux rope field lines; meanwhile, they are heated by the reconnection.

5. Discussions

The light bridge that we study has many characteristics similar to those reported in previous studies. For example, Ruedi et al. (1995) and Leka (1997) showed that the magnetic field in the light bridge is more inclined and the total magnetic field strength there is weaker relative to those at the surrounding umbra, which are exactly the features we demonstrate here. The

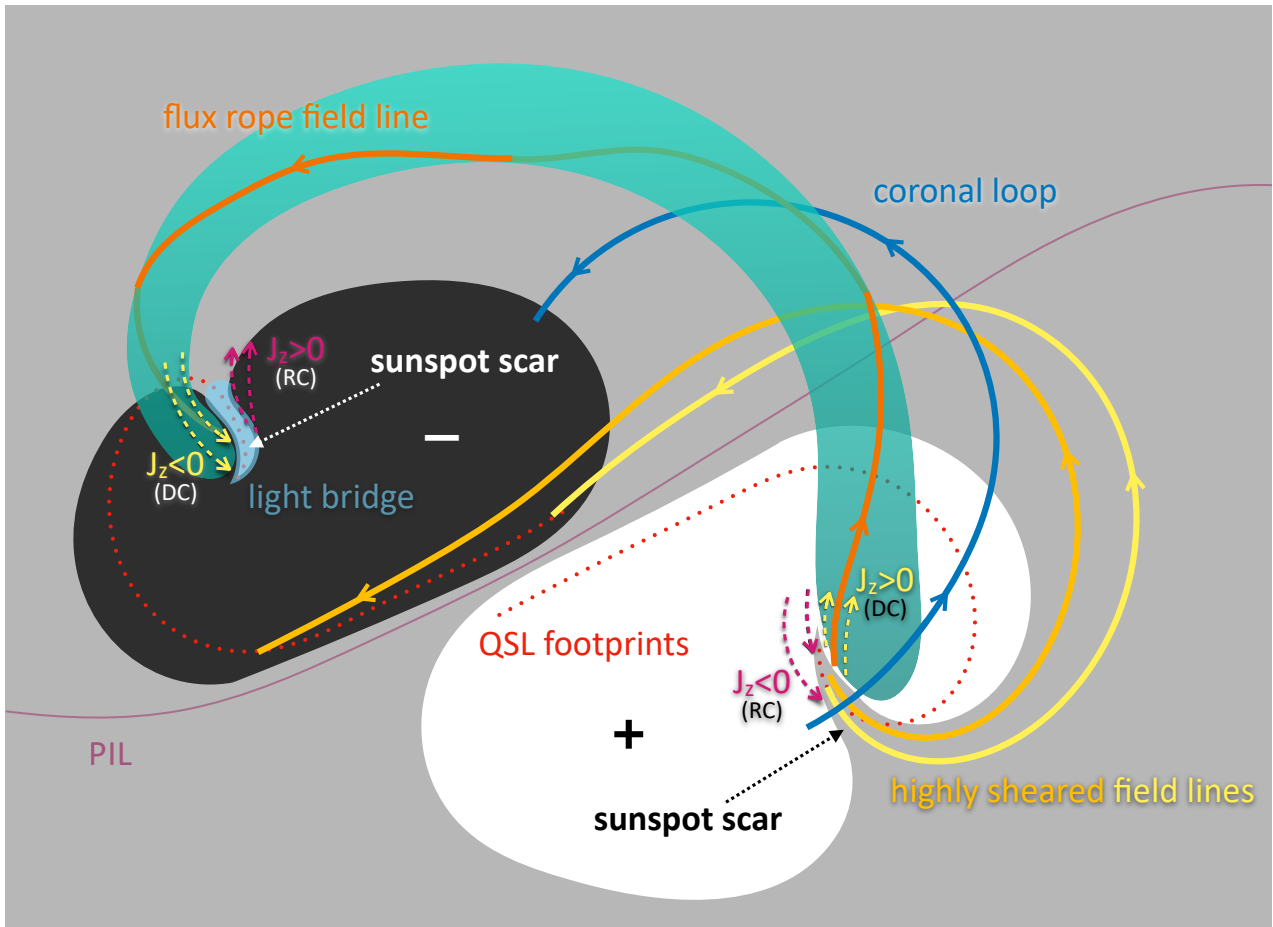


Fig. 13. Sketch of the sunspot scar. The white and black regions represent the positive and negative polarities in an active region, which are separated by the PIL (the purple solid curve). The sunspot scars are shown as the arc-shaped intrusions in the positive and negative polarities. We only show the light bridge which is co-spatial with the sunspot scar in the negative polarity, while the light bridge could also appear in the positive one although not shown. In the positive polarity, we show the flux rope (represented by the green tube and also the dark orange field line in it) anchored at the inner side of the sunspot scar, the coronal loop (blue field line) rooted at the outer side, and the highly sheared field lines (light orange and yellow field lines) whose one footpoint is in the sunspot scar and the other one is on the QSL footprints (shown by the red dashed curves) in the other polarity. Similarly, the above field lines also exist around the sunspot scar in the negative polarity although not shown. The yellow and purple dashed arrows at two sides of the sunspot scars represent the direct current (DC) in the forward-S flux rope and the return current (RC) in the shielding background coronal loops, respectively.

previous studies generally interpret the light bridge as the field-free (or weak-field) material intruding into the umbra by upward convection; the surrounding umbral fields gather above and cover the intrusive material in a shape of canopy (Leka 1997; Toriumi et al. 2015). However, here we show that this specific narrow and curved light bridge is more closely related to the highly inclined and sheared field lines which are in the process of slipping reconnection and at the transition between the flux rope field lines and the background coronal loops. This result, which is obviously different from the previous explanation, provides a new perspective for understanding the nature of at least some light bridges.

Our results also have implications for understanding the heating in the pre-eruptive structure. As demonstrated in the observation (Cheng et al. 2023) and the simulation (Xing et al., in prep.), the magnetic reconnection in current sheets under (and sometimes also surrounding) the pre-eruptive flux rope could heat the local plasma while forming twisted flux rope field lines. These newly-formed hot field lines are added into the pre-eruptive flux rope and thus contribute to its heating. Here, using both the observation and the simulation, we show that magnetic

field lines are actually gradually heated when they evolve from coronal loops to flux rope field lines. In particular, both of these two processes are closely related to the slipping reconnection. This indicates that no matter for the entire flux rope or for a certain field line in it, the heating by reconnection is a gradual rather than instantaneous process, which enriches our understandings in Cheng et al. (2023) and Xing et al. (in prep.).

As mentioned in Sect. 1, there are two methods to identify the flux rope footpoint: one with the flare ribbon hook and the other with the core dimming. However, both of these two methods face many difficulties in their applications to observations. First, for the flare ribbon hook method, the hook in the observation is usually partially closed. Therefore, it is elusive to determine the boundary of the flux rope footpoint at the unclosed section of the hook with this method.

Second, for the core dimming method, the dimming regions before the eruption (Qiu & Cheng 2017; Wang et al. 2019, 2023) and during the eruption (Qiu et al. 2007; Dissauer et al. 2018) are usually determined by empirical thresholds for the emission intensity. The uncertainty of the empirical threshold and the use of a constant threshold during the whole evolution of an event

may bring errors to the identification of the footpoint. In particular, the footpoints before the eruption determined in these works are usually fixed. However, the real footpoint should evolve and move with the evolution of the pre-eruptive flux rope (as the observational event in this work). In addition, due to a lack of flare ribbon hooks before the eruption, it is no longer possible to limit the empirical threshold of the pre-flare dimming by the ribbon hook as what Xing et al. (2020) did for the dimming region during the eruption.

We suggest that the sunspot scar could alleviate the problems above. For both the pre-eruptive and eruptive flux ropes, the sunspot scar is expected to help (a) directly show the footpoint edge and (b) indirectly determine the footpoint by limiting the threshold or area of the core dimming region, the latter of which is previously only available with clear ribbon hooks during the eruption (e.g., Wang et al. 2017; Xing et al. 2020).

It should be pointed out that the observation and the simulations studied in this work are all in the framework of “pre-eruptive structures being flux ropes.” Therefore, the views we put forward, that the sunspot scar before the eruption represents the edge of the pre-eruptive flux rope footpoint and that the drifting of the former represents the growth and deformation of the pre-eruptive flux rope, are also within this framework. However, the pre-eruptive structure is also suggested to be a sheared arcade system for some CME events (Antiochos et al. 1994; DeVore & Antiochos 2000; Song et al. 2014; Ouyang et al. 2015). Future works ought to study whether the sunspot scar also exists in the pre-eruptive stage of events in which the pre-eruptive structures are sheared arcades and, if so, what the nature of this type of sunspot scar would be.

We note that sunspot scars are not always observed even in CME-flare events with flux ropes. A reasonable speculation to explain such a rarity is: although the decrease of B_z and also other features at the edge of the flux rope footpoint may exist in many events, sunspot scars may be not visible when: (1) their features are not as strong as those in the event on July 12, 2012 or (2) their features are covered up by the features of surrounding magnetic field when the edge of the flux rope footpoint is located in faculae or penumbra rather than umbrae. This speculation needs to be examined by more investigations on the conditions of formation and observability of sunspot scars in the future.

However, it should also be mentioned that the sunspot scar is not a unique structure existing only in the event on July 12, 2012. For example, although not as clear as the event that we studied, there is also a “sunspot-scar-like” structure in the active region NOAA 11818, which is the source region of a CME-flare event on August 17, 2013 (see Figs. 1 and 6 in Zhang et al. 2022). It is thus expected that more events with sunspot scars could be discovered in the future, with our work as a starting point. On the basis of more events, the sunspot scar may offer a new opportunity for the ground-based telescopes (e.g., DKIST, WeHoST, and future EST) to study the properties and evolution of flux ropes related to CMEs, as the sunspot scar and its related light bridge are observable with photosphere-polarimetry instruments in general and with ground-based instruments in particular.

Acknowledgements. C.X. and G.A. acknowledge financial support from the French national space agency (CNES), as well as from the Programme National Soleil Terre (PNST) of the CNRS/INSU also co-funded by CNES and CEA. C.X. also acknowledges financial support from China Scholarship Council. G.A. thanks the Croom team for fruitful discussions. X.C. and M.D.D. are supported by National Key R&D Program of China under grants 2021YFA1600504 and NSFC under grant 12127901. Solar Dynamics Observatory (SDO) is a mission of NASA’s Living With a Star Program. Simulations analyzed in this work were performed on the HPC center MesoPSL which is financed by the Région Île-de-France and the project Equip@Meso of the PIA supervised by the ANR, the

computing facilities in High Performance Computing Center of Nanjing University, and the Cholesky computing cluster from the IDCS mesocentre at Ecole Polytechnique.

References

- Antiochos, S. K., Dahlburg, R. B., & Klimchuk, J. A. 1994, *ApJ*, 420, L41
Aulanier, G. 2016, *Nat. Phys.*, 12, 998
Aulanier, G., & Démoulin, P. 1998, *A&A*, 329, 1125
Aulanier, G., & Dudík, J. 2019, *A&A*, 621, A72
Aulanier, G., Démoulin, P., & Grappin, R. 2005, *A&A*, 430, 1067
Aulanier, G., Török, T., Démoulin, P., et al. 2010, *ApJ*, 708, 314
Aulanier, G., Janvier, M., & Schmieder, B. 2012, *A&A*, 543, A110
Barczynski, K., Aulanier, G., Masson, S., et al. 2019, *ApJ*, 877, 67
Chen, J., Howard, R. A., Brueckner, G. E., et al. 1997, *ApJ*, 490, L191
Cheng, X., & Ding, M. D. 2016, *ApJS*, 225, 16
Cheng, J. X., & Qiu, J. 2016, *ApJ*, 825, 37
Cheng, X., Zhang, J., Saar, S. H., et al. 2012, *ApJ*, 761, 62
Cheng, X., Ding, M. D., Zhang, J., et al. 2014, *ApJ*, 789, 93
Cheng, X., Guo, Y., & Ding, M. 2017, *Sci. China Earth Sci.*, 60, 1383
Cheng, X., Zhang, J., Kliem, B., et al. 2020, *ApJ*, 894, 85
Cheng, X., Xing, C., Aulanier, G., et al. 2023, *ApJ*, 954, L47
Dedner, A., Kemm, F., Kröner, D., et al. 2002, *J. Comput. Phys.*, 175, 645
Démoulin, P., Priest, E. R., & Lonie, D. P. 1996, *J. Geophys. Res.*, 101, 7631
Dere, K. P., Brueckner, G. E., Howard, R. A., et al. 1999, *ApJ*, 516, 465
DeVore, C. R., & Antiochos, S. K. 2000, *ApJ*, 539, 954
Dissauer, K., Veronig, A. M., Temmer, M., et al. 2018, *ApJ*, 855, 137
Dudík, J., Janvier, M., Aulanier, G., et al. 2014, *ApJ*, 784, 144
Elovaara, J. 2007, *Space Weather : Research Towards Applications in Europe 2nd European Space Weather Week (ESWW2)*, 344, 311
Gou, T., Liu, R., Veronig, A. M., et al. 2023, *Nat. Astron.*, 7, 815
Guo, Y., Ding, M. D., Schmieder, B., et al. 2010, *ApJ*, 725, L38
Guo, J. H., Ni, Y. W., Zhong, Z., et al. 2023, *ApJS*, 266, 3
Harra, L. K., & Sterling, A. C. 2001, *ApJ*, 561, L215
Janvier, M., Aulanier, G., Pariat, E., et al. 2013, *A&A*, 555, A77
Janvier, M., Aulanier, G., Bommier, V., et al. 2014, *ApJ*, 788, 80
Kliem, B., & Török, T. 2006, *Phys. Rev. Lett.*, 96, 255002
Leka, K. D. 1997, *ApJ*, 484, 900
Lemen, J. R., Title, A. M., Akin, D. J., et al. 2012, *Sol. Phys.*, 275, 17
Liu, C., Deng, N., Liu, Y., et al. 2005, *ApJ*, 622, 722
Lörinčák, J., Dudík, J., & Aulanier, G. 2019, *ApJ*, 885, 83
Lörinčák, J., Dudík, J., Aulanier, G., et al. 2021, *ApJ*, 906, 62
McCauley, P. I., Su, Y. N., Schanche, N., et al. 2015, *Sol. Phys.*, 290, 1703
Ouyang, Y., Yang, K., & Chen, P. F. 2015, *ApJ*, 815, 72
Patsourakos, S., Vourlidas, A., Török, T., et al. 2020, *Space Sci. Rev.*, 216, 131
Pessnell, W. D., Thompson, B. J., & Chamberlin, P. C. 2012, *Sol. Phys.*, 275, 3
Priest, E. R., & Démoulin, P. 1995, *J. Geophys. Res.*, 100, 23443
Qiu, J., & Cheng, J. 2017, *ApJ*, 838, L6
Qiu, J., Hu, Q., Howard, T. A., et al. 2007, *ApJ*, 659, 758
Rueddi, I., Solanki, S. K., & Livingston, W. 1995, *A&A*, 302, 543
Savcheva, A., Pariat, E., McKillop, S., et al. 2015, *ApJ*, 810, 96
Scherer, P. H., Schou, J., Bush, R. I., et al. 2012, *Sol. Phys.*, 275, 207
Schmieder, B., & Aulanier, G. 2018, *Electric Curr. Geospace Beyond*, 235, 391
Schmieder, B., Démoulin, P., & Aulanier, G. 2013, *Adv. Space Res.*, 51, 1967
Song, H. Q., Zhang, J., Chen, Y., et al. 2014, *ApJ*, 792, L40
Sterling, A. C., & Hudson, H. S. 1997, *ApJ*, 491, L55
Su, Y., Surges, V., van Ballegoijen, A., et al. 2011, *ApJ*, 734, 53
Sun, X., Hoeksema, J. T., Liu, Y., et al. 2012, *ApJ*, 748, 77
Tian, H., McIntosh, S. W., Xia, L., et al. 2012, *ApJ*, 748, 106
Titov, V. S., Hornig, G., & Démoulin, P. 2002, *J. Geophys. Res. (Space Phys.)*, 107, 1164
Titov, V. S., Downs, C., Török, T., et al. 2021, *ApJS*, 255, 9
Toriumi, S., Katsukawa, Y., & Cheung, M. C. M. 2015, *ApJ*, 811, 137
Wang, W., & Liu, R. 2021, *A&A*, 647, A108
Wang, S., Liu, C., & Wang, H. 2012a, *ApJ*, 757, L5
Wang, H., Deng, N., & Liu, C. 2012b, *ApJ*, 748, 76
Wang, W., Liu, R., Wang, Y., et al. 2017, *Nat. Commun.*, 8, 1330
Wang, W., Zhu, C., Qiu, J., et al. 2019, *ApJ*, 871, 25
Wang, W., Qiu, J., Liu, R., et al. 2023, *ApJ*, 943, 80
Xia, C., Teunissen, J., El Mellah, I., et al. 2018, *ApJS*, 234, 30
Xing, C., Cheng, X., & Ding, M. D. 2020, *The Innovation*, 1, 100059.
Zhang, J., Cheng, X., & Ding, M.-D. 2012, *Nat. Commun.*, 3, 747
Zhang, J., Xu, Z., Zhang, Q., et al. 2022, *ApJ*, 933, L20
Zhao, J., Gilchrist, S. A., Aulanier, G., et al. 2016, *ApJ*, 823, 62
Zuccarello, F. P., Aulanier, G., & Gilchrist, S. A. 2015, *ApJ*, 814, 126

Appendix A: Details of “Simulation 2”

In the following, we introduce the setups of “Simulation 2” and also the kinematics of the flux rope in this simulation. We refer readers to “Simulation Ue” in Xing et al. (in prep.) for more details.

A.1. Equations and grids

“Simulation 2” is performed by the code MPI-AMRVAC (Xia et al. 2018) by solving the following equations:

$$\frac{\partial \rho}{\partial t} + \nabla \cdot (\rho \mathbf{v}) = 0, \quad (\text{A.1})$$

$$\frac{\partial (\rho \mathbf{v})}{\partial t} + \nabla \cdot [\rho \mathbf{v} \mathbf{v} + (p + \frac{\mathbf{B}^2}{2\mu_0}) \mathbf{I} - \frac{\mathbf{B} \mathbf{B}}{\mu_0}] = \rho \mathbf{g} + 2\mu \nabla \cdot [\mathbf{S} - \frac{1}{3}(\nabla \cdot \mathbf{v}) \mathbf{I}], \quad (\text{A.2})$$

$$\frac{\partial \mathbf{B}}{\partial t} + \nabla \cdot (\mathbf{v} \mathbf{B} - \mathbf{B} \mathbf{v} + \psi \mathbf{I}) = -\nabla \times (\eta \mathbf{J}), \quad (\text{A.3})$$

$$\frac{\partial e_{\text{int}}}{\partial t} + \nabla \cdot (e_{\text{int}} \mathbf{v}) = -p \nabla \cdot \mathbf{v} + 2\mu [\mathbf{S} : \mathbf{S} - \frac{1}{3}(\nabla \cdot \mathbf{v})^2] + \eta J^2 + \nabla \cdot [\kappa_{\parallel} (\mathbf{b} \cdot \nabla T) \mathbf{b}], \quad (\text{A.4})$$

$$\nabla \times \mathbf{B} = \mu_0 \mathbf{J}, \quad (\text{A.5})$$

$$\frac{\partial \psi}{\partial t} + c_h^2 \nabla \cdot \mathbf{B} = -\frac{c_h^2}{c_p^2} \psi. \quad (\text{A.6})$$

The equations are solved in the dimensionless form. The magnetic permeability μ_0 is set to 1. The dimensionless unit of the length, time (t), mass density (ρ), thermal pressure (p), internal energy (e_{int}), temperature (T), velocity (\mathbf{v}) magnitude, and magnetic field (\mathbf{B}) strength is 10 Mm, 67.89 s, 2.34×10^{-15} g cm $^{-3}$, 0.51 erg cm $^{-3}$, 0.51 erg cm $^{-3}$, 1.6 MK, 147.30 km s $^{-1}$, and 2.53 G, respectively. \mathbf{J} is the current density. $\mathbf{g} = -g\mathbf{e}_z$ represents the gravity acceleration. μ , the dynamic viscosity coefficient, is set to 10^{-4} in dimensionless unit, and η is the resistivity coefficient. κ_{\parallel} is the parallel conductivity coefficient and equals to $8 \times 10^{-7} T^{5/2}$ erg cm $^{-1}$ s $^{-1}$ K $^{-1}$. \mathbf{S} is the strain tensor and \mathbf{I} is the unit tensor. $\mathbf{b} = \mathbf{B}/B$ is the normalized magnetic field. The zero divergence condition of the magnetic field is maintained with the generalized Lagrange multiplier (GLM) method (Dedner et al. 2002) by introducing a parameter ψ , the evolution of which follows Eq. A.6.

The physical domain of the simulation, in the range of -70 Mm $\leq x \leq 70$ Mm, -70 Mm $\leq y \leq 70$ Mm, and 0 Mm $\leq z \leq 140$ Mm, is resolved by a stretched grid $n_x \times n_y \times n_z = 144 \times 144 \times 96$. The finest spatial resolutions in three directions are all about 300 km.

A.2. Initial conditions and boundary conditions

The initial magnetic field is set to a potential bipolar field:

$$\begin{aligned} B_x(t=0) &= \sum_{m=1}^4 c_m (x - x_m) r_m^{-3} \\ B_y(t=0) &= \sum_{m=1}^4 c_m (y - y_m) r_m^{-3} \\ B_z(t=0) &= \sum_{m=1}^4 c_m (z - z_m) r_m^{-3} \end{aligned} \quad (\text{A.7})$$

$$r_m = \sqrt{(x - x_m)^2 + (y - y_m)^2 + (z - z_m)^2},$$

where $(c_1 = 60, x_1 = 0.9, y_1 = 0.3, z_1 = -1.1)$, $(c_2 = -60, x_2 = -0.9, y_2 = -0.3, z_2 = -1.1)$, $(c_3 = 45, x_3 = 9, y_3 = 3, z_3 = -11)$, and $(c_4 = -45, x_4 = -9, y_4 = -3, z_4 = -11)$ in dimensionless units.

The initial atmosphere is set to a hydrostatic corona with a uniform temperature of 1.6 MK. The initial mass density on the plane $z = 0$, which corresponds to 3 Mm above the solar surface, is set to 2.34×10^{-15} g cm $^{-3}$. The initial velocity and parameter ψ are set to zero.

We set line-tied boundary conditions for the bottom boundary, open boundary conditions for the top boundary, and closed boundary conditions for the four side boundaries. Here, the line-tied conditions mean that the footpoints of field lines can only move horizontally following the prescribed motions in the condition of ideal MHD (Aulanier et al. 2005). We refer readers to Xing et al. (in prep.) for more details of boundary conditions.

A.3. Driving motions

In “Simulation 2”, to drive the magnetic field and form a flux rope, two types of line-tied motions are imposed at the cell-center bottom surface which is a horizontal surface ($z = 0.015$) at the altitude of the cell center of the layer $k = 1$ (cell layers in physical domain indexed by $k = 1, 2, 3, \dots, 96$ from the bottom to the top). According to types of driving motions, the simulation is divided into three phases: the shearing phase ($0 \leq t \leq 18$) with a shearing motion (v_x^s, v_y^s, v_z^s) applied to drive the initial potential field to a highly sheared state:

$$\begin{aligned} v_x^s(k=1; t) &= \gamma(t) V_x^s(t), \\ v_y^s(k=1; t) &= \gamma(t) V_y^s(t), \\ v_z^s(k=1; t) &= 0, \\ V_x^s(t) &= 0.16 \Psi_0(t) \partial_y \Psi(t), \\ V_y^s(t) &= -0.16 \Psi_0(t) \partial_x \Psi(t), \end{aligned} \quad (\text{A.8})$$

$$\gamma(t) = \begin{cases} \frac{1}{2} \tanh[3.75(t-1)] + \frac{1}{2} & 0 \leq t < 16, \\ -\frac{1}{2} \tanh[3.75(t-17)] + \frac{1}{2} & 16 \leq t \leq 18, \end{cases}$$

$$\Psi(t) = \exp[-5.5 \left(\frac{B_z(k=1; t)}{B_z^{\text{max}}(k=1; t)} \right)^2],$$

the converging phase ($18 < t \leq 60$) with a converging motion (v_x^c, v_y^c, v_z^c) applied to form a flux rope by the flux cancellation:

$$\begin{aligned}
 v_x^c(k=1; t) &= \gamma(t)V_x^c(t), \\
 v_y^c(k=1; t) &= \gamma(t)V_y^c(t), \\
 v_z^c(k=1; t) &= 0, \\
 V_x^c(t) &= 0.16\Psi_0(t)\partial_x\Psi(t), \\
 V_y^c(t) &= 0.16\Psi_0(t)\partial_y\Psi(t), \\
 \gamma(t) &= \begin{cases} \frac{1}{2}\tanh[3.75(t-19)] + \frac{1}{2} & 18 < t \leq 59, \\ -\frac{1}{2}\tanh[6.0(t-59.5)] + \frac{1}{2} & 59 < t \leq 60, \end{cases} \\
 \Psi(t) &= \exp[-27.5(\frac{B_z(k=1; t)}{B_z^{max}(k=1; t)})^2],
 \end{aligned} \tag{A.9}$$

and the relaxation phase ($60 < t \leq 71$) in which the velocity in the layer $k=1$ is fixed to zero to relax the whole system. It should be noted that Eqs. A.8 and A.9 are in dimensionless form.

Correspondingly, in the layer $k=1$, the dissipation term in Eq. A.3 is modified into:

$$\frac{\partial \mathbf{B}}{\partial t} + \nabla \cdot (\mathbf{v}\mathbf{B} - \mathbf{B}\mathbf{v} + \psi\mathbf{I}) = \begin{cases} 0 & 0 \leq t \leq 18, \\ \eta(\frac{\partial^2}{\partial x^2} + \frac{\partial^2}{\partial y^2})\mathbf{B} & 18 < t \leq 60, \\ 0 & 60 < t \leq 71. \end{cases} \tag{A.10}$$

During the shearing phase and relaxation phase, there is no dissipation term in the layer $k=1$ to fulfill the line-tied condition; the dimensionless resistivity is set to 10^{-4} in the whole region except the layer $k=1$. During the converging phase, a two-dimensional (2D) dissipation term (Aulanier et al. 2010) is set in the layer $k=1$ to allow the flux cancellation close to the PIL; the dimensionless resistivity is set to 4×10^{-4} in the whole region including the layer $k=1$.

A.4. Kinematics of the flux rope

The kinematics of the flux rope in ‘‘Simulation 2’’ is estimated by measuring the height of the apex of an overlying field line right above the flux rope. The overlying field line is traced from a point at the center of the positive polarity and on the cell-center bottom surface. The velocity at this point is quite small or even zero in all phases, which ensures that this field line could well reflect the kinematics of the flux rope.

The height evolution of the flux rope before and during the eruption ($52 \leq t \leq 71$) is shown in Fig. A.1. The onset time of the CME in the observational sense, that is, the start time of the exponential rise of the CME, is determined with methods in McCauley et al. (2015) and Cheng et al. (2020). The evolution of the height (h) of the flux rope with the time (t) in Fig. A.1 is fitted by a function $h = ae^{bt} + ct + d$, which is composed of an exponential term $h_e = ae^{bt}$ and a linear term $h_l = ct + d$. The start time of the exponential rise is defined at $t = \ln(c/ab)/b$, after which the velocity contributed by the exponential term, $v_e = abe^{bt}$, exceeds that contributed by the linear term, $v_l = c$. For ‘‘Simulation 2’’, this start time is at $t = 68.5$, marked by the blue dashed line in Fig. A.1.

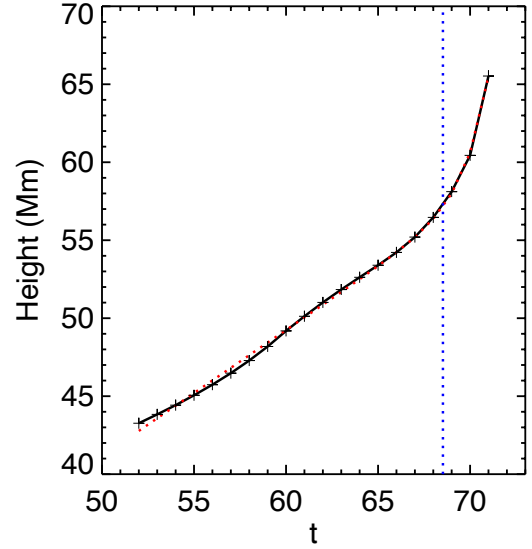


Fig. A.1. Kinematics of the flux rope in ‘‘Simulation 2.’’ The black points and the black curve represent the evolution of the measured height of the (pre-)eruptive structure, and the red dashed curve is the best fitting curve of the measured height-time data. The vertical dashed line marks the start time of the exponential rise of the CME.